

# Modelling Cell Invasion in the Neural Crest



Thomas Pak  
Brasenose College  
University of Oxford

Dissertation submitted in partial fulfilment of the requirements for  
the degree of

*M.Sc. in Mathematical Modelling and Scientific Computing*

Trinity Term 2017

*“Somewhere, something incredible is waiting to be known.”*

— Carl Sagan

## Acknowledgements

First and foremost, I would like to thank Professor Philip Maini for agreeing to supervise this dissertation. It was truly an honour and a pleasure to receive guidance from someone who is, at once, a world-class expert and a wonderful person.

I am also thankful to the MMSC course director Dr Kathryn Gillow for the overwhelming support that she has provided to the MMSC this past year. She always went beyond and above to help us in every way possible, and I could not start to conceive the horrors that would have unfolded if she was not our course director!

I would also like to thank the receptionists at the Mathematical Institute, who were always ready to assist in many little, but significant ways. When life was tough, they made it easy.

Thanks to the MMSC for trusting that I would make the MMSC great again and electing me to be their President. I cannot imagine a more amazing collection of wonderful individuals that I could have spent this year with. Special thanks to the people who contributed to making MMSC great again: Réka and Bertie for being the best Social Secretary and honorary Social Secretary a President could ever wish for; Marius, Federica and Rodrigo for their roles in organising not one, but two amazing MMSC formals; and finally François and John for the extreme passion with which they fulfilled their roles (which shall not be made explicit here).

None of this would be possible without the support of my parents, who have always encouraged me to explore my full potential.

Finally, I want to thank my girlfriend Pamika for being the light in my life. I would not be half the man I am today if it was not for her endless support and love.

# Abstract

During vertebrate embryogenesis, a special type of cells, called the neural crest cells, migrate from the neural tube and invade many distant regions of the developing embryo, where they contribute to the development of the peripheral nervous system, the adrenal glands and the skeletal structure of the face, amongst others. Despite their central importance in vertebrate development, it is unclear how they achieve persistent migration over long distances. Studies of cranial neural crest cells that combined cell-based modelling with *in vivo* experiments have demonstrated that their migration relies on the interaction of at least two distinct subpopulations [1, 2]. In this model, the leading edge of the migratory stream is populated by a leader cell type that responds chemotactically to a cell-induced chemotactic gradient, while a follower cell type trails the leaders by cell to cell contact in a formation resembling a conga line. Gene expression profiling experiments then showed that the front and trailing cells expressed different genes related to cell guidance and navigation.

In this dissertation, we study the implications of a leader–follower dynamic in a continuum model based on partial differential equations. First, we demonstrate that a leader–follower model with fixed subpopulations does not result in any noticeable improvements. However, when cells are allowed to switch between leader and follower phenotypes, the cell population self-organises into highly directed wavefront, extending the range and robustness of cell migration. Moreover, we show that the leader–follower principle can be applied iteratively to an arbitrary number of cell types to form a chain of interacting subpopulations. This is in agreement with recent experiments that show there is a spectrum of differential gene expression along the neural crest migration pathway.

# Contents

|          |   |           |
|----------|---|-----------|
| <b>1</b> | <b>Introduction</b>                           | <b>1</b>  |
| 1.1      | Neural Crest Migration . . . . .              | 2         |
| 1.2      | Outline . . . . .                             | 5         |
| <b>2</b> | <b>Chemotaxis</b>                             | <b>6</b>  |
| 2.1      | Signal-Dependent Sensitivity (SDS) . . . . .  | 7         |
| 2.1.1    | Receptor Model . . . . .                      | 8         |
| 2.1.2    | Logarithmic Model . . . . .                   | 10        |
| 2.2      | Forced Versus Cell-Induced Gradient . . . . . | 12        |
| <b>3</b> | <b>Leader Model</b>                           | <b>15</b> |
| 3.1      | Necessity of Singular Chemotaxis . . . . .    | 17        |
| 3.2      | Travelling Wave Analysis . . . . .            | 18        |
| 3.3      | Discussion . . . . .                          | 21        |
| 3.4      | Failure of Non-Singular Chemotaxis . . . . .  | 26        |
| <b>4</b> | <b>Leader–Follower Model</b>                  | <b>28</b> |
| 4.1      | Failure of Fixed Subpopulations . . . . .     | 29        |
| 4.2      | Cell Differentiation . . . . .                | 33        |
| 4.2.1    | Leader-Induced Cell-Crowding . . . . .        | 34        |
| 4.2.2    | Self-Organisation . . . . .                   | 36        |
| 4.3      | Cell Flux Analysis . . . . .                  | 37        |
| 4.3.1    | Indirect Model . . . . .                      | 40        |
| 4.4      | Discussion . . . . .                          | 41        |
| <b>5</b> | <b>Chain Model</b>                            | <b>44</b> |
| 5.1      | Generalisation of Indirect Model . . . . .    | 45        |
| 5.2      | Cell Flux Analysis . . . . .                  | 47        |

|                          |           |
|--------------------------|-----------|
| 5.3 Discussion . . . . . | 51        |
| <b>6 Conclusions</b>     | <b>53</b> |
| <b>A Parameters</b>      | <b>55</b> |
| <b>References</b>        | <b>60</b> |

# List of Figures

|     |  |    |
|-----|--|----|
| 1.1 | Formation and migration of NC cells. . . . .   | 3  |
| 1.2 | Leader–follower model of cranial NC cell migration . . . . .   | 4  |
| 2.1 | Receptor model. . . . .  | 9  |
| 2.2 | Illustration of Weber–Fechner’s law. . . . .   | 10 |
| 2.3 | Logarithmic model. . . . .   | 12 |
| 2.4 | Forced chemoattractant gradient. . . . .   | 14 |
| 3.1 | Leader model with naive boundary conditions. . . . .   | 22 |
| 3.2 | Leader model with Robin boundary conditions. . . . .   | 24 |
| 3.3 | Leader model without chemoattractant diffusion. . . . .  | 25 |
| 3.4 | Failure of leader model for non-singular logarithmic chemotaxis. . . .   | 26 |
| 3.5 | Failure of leader model with receptor law. . . . .   | 27 |
| 4.1 | Results for direct leader–follower model without and with conversion.  | 31 |
| 4.2 | Profiles for direct leader–follower model without and with conversion.   | 32 |
| 4.3 | Comparison of profiles for leader-only versus follower-only flux in direct<br>leader–follower model with conversion. . . . . | 35 |
| 4.4 | Comparison of conversion versus no conversion in direct leader–follower<br>model without boundary cell fluxes. . . . .       | 37 |
| 4.5 | Flux analysis of direct leader–follower model. . . . .   | 39 |
| 4.6 | Comparison of profiles in direct versus indirect leader–follower model.  | 40 |
| 4.7 | Flux analysis of indirect leader–follower model. . . . .   | 42 |
| 5.1 | Flux analysis of chain model . . . . .   | 49 |
| 5.2 | Scaled flux analysis for chain model with 9 cell types. . . . .  | 50 |
| 5.3 | Flux analysis of individual cell types for chain model 9 cell types. . .   | 50 |
| 5.4 | Profiles for chain model with 9 cell types. . . . .  | 51 |

# List of Tables

|     |   |    |
|-----|---|----|
| 2.1 | Chemotaxis models. . . . .                                    | 8  |
| A.1 | Parameters for forced chemoattractant gradient model. . . . . | 56 |
| A.2 | Parameters for leader model. . . . .                          | 56 |
| A.3 | Parameters for direct leader–follower model. . . . .          | 57 |
| A.4 | Parameters for indirect leader–follower model. . . . .        | 58 |
| A.5 | Parameters for chain model. . . . .                           | 59 |



# Chapter 1

## Introduction

An amazing fact of biology is that every multicellular organism starts out as a single cell. From these humble beginnings, an incredibly diverse array of cell types arise that form the intricate system of tissues and organs that constitutes complex lifeforms such as humans. Embryogenesis is the process that starts after fertilisation and results in a mature embryo. This is not a straightforward task considering that the embryo possesses the essential features and structural characteristics of its corresponding adult lifeform. If the genetic code can be thought of as the blueprint of an organism, then the embryo is its living prototype, complete with limbs, brains and a beating heart.

One of the main challenges of embryogenesis is essentially a game of numbers. A fertilised egg cell is just one cell, while a fully developed human baby contains on the order of trillions of cells. Hence, cell division is a crucial driver of embryonic development. As cells become more numerous, they start assuming distinct morphologies and specialised roles in a process called cell differentiation. A carefully orchestrated cascade of cell division and differentiation should then form an embryo with a well-defined structure.

However, it turns out that embryogenesis cannot be explained solely by cell division and differentiation. Experiments have shown that cells are not necessarily confined to their place of origin in the embryo and that they can migrate to other regions of the developing body to form adult structures. In particular, the neural tube, which is the precursor of the spine in vertebrate animals, sheds cells from its crest that migrate into the rest of the embryo. These neural crest (NC) cells then divide and differentiate to give rise to a very diverse cell lineage. They play crucial roles in the development of the peripheral nervous system, the heart and many other organs [3].

The importance of studying NC cells is twofold. On the one hand, understanding the mechanisms that drive NC cell migration provides insight to the process of embryogenesis as a whole and can elucidate the causes of certain congenital disorders. On the other hand, highly aggressive cancers such as melanoma and neuroblastoma originate from NC-derived cell populations. Moreover, their migratory patterns resemble those of NC cells during embryogenesis [4]. Advances in NC cell research could thus have implications for cancer research as well.

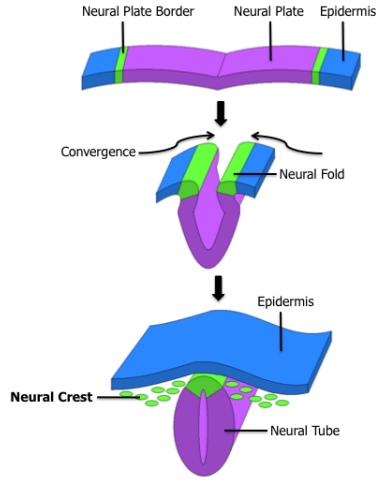
Biological systems typically display emergent, collective properties that arise from the interactions of many individuals. This is especially the case for interacting cell populations. Thus, even if the behaviour of individuals is perfectly characterised, it is difficult to make predictive statements about phenomena on the system level. This explains the need for mathematical models and computational methods in biology [5, 6]. Simplified models that distil the system to its key components and interactions often provide crucial analytical insights into the system. More elaborate models that preclude analysis are still valuable as predictive *in silico* models for testing hypotheses and guiding experiments.

In this dissertation, we build upon an individual-based model (IBM) that was previously developed for the migration of cranial NC cells [7, 1, 2]. Even though the model agrees with experiments on chick embryos and is successful in making experimentally validated predictions, mathematical analysis is intractable because of the individual-based component. The aim of this dissertation is thus to construct a suite of models based on partial differential equations (PDEs) for cranial NC cell migration and analyse its properties.

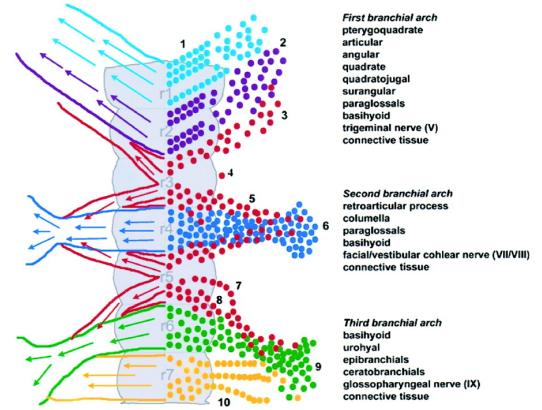
In the next section, a short introduction of the neural crest and existing models for NC cell migration is given. This is followed by a brief discussion of the IBM for cranial NC cells. The final section provides an overview of the overall approach of this work and outlines the structure of the dissertation.

## 1.1 Neural Crest Migration

After gastrulation, the early vertebrate embryo consists of three differentiated germ layers, the ectoderm, mesoderm and endoderm. The neural tube is formed when part of the ectoderm sinks into the mesoderm and the neural folds converge (see Figure 1.1a). The crest of the neural tube, where the neural folds converge, subsequently releases NC cells that invade various parts of the embryo. The migration of NC cells is strongly regulated and occurs in discrete, multicellular streams (see Figure 1.1b).



(a) Formation of the neural crest.



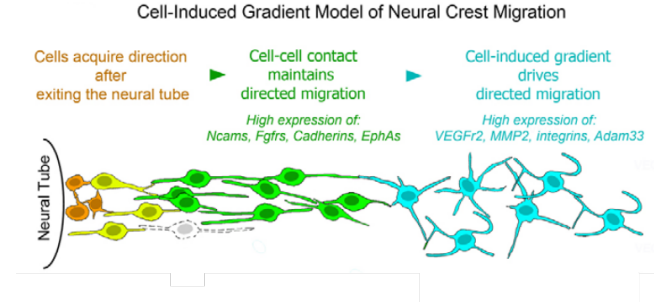
(b) Migratory paths and fates of cranial NC cells.

Figure 1.1: Formation and migration of NC cells (reproduced from [8] and [9]).

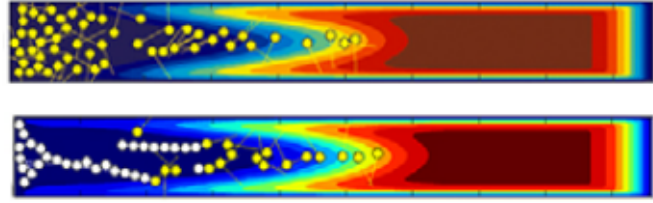
Extensive studies have been able to map the pathways of NC cells originating in different regions of the neural tube and have also identified the corresponding cell fates [3]. The mechanism of cell migration is not uniform along the neural tube, and it is better characterised for some types of NC cells than others. For example, it has been shown that enteric NC cells rely on proliferation to populate the intestinal tract [10]. Further mathematical modelling supports the hypothesis that Hirschsprung’s disease is caused by a mismatch between the gut growth and NC cell invasion [11].

By contrast, proliferation does not play a significant role during invasion by cranial NC cells. Instead, the IBM suggests that a directed NC cell stream is achieved by having a distinct “leader” cell type respond to a chemoattractant, while the “follower” cell type latches on to leaders or other followers by cell–cell contact, thus creating a formation resembling a conga line (Figure 1.2a). Indeed, experiments have revealed that the NC cells at the leading edge of the invasive front express different genes than the trailing cells [1, 2].

The IBM model was simulated on a rectangular, growing domain with the concentration of the chemoattractant, vascular endothelial growth factor (VEGF), governed by a reaction–diffusion equation. Leading cells on the other hand were represented by non-overlapping discs that periodically sampled VEGF in their local environment and moved only if they sensed a favourable VEGF gradient. This chemoattractant gradient was created by the consumption of VEGF by the NC cells [12]. As a result, the leading cells migrate in a directed manner as a result of a cell-induced gradient



(a) Proposed mechanism of cranial NC cell migration.



(b) IBM simulation in 2D. Heat map indicates VEGF concentration, Yellow discs are leaders and white discs are followers. In the top panel, it is assumed only leaders are present, while in the bottom panel there are leaders and followers. In both cases there is invasion of the domain, but in the leader model the cells become stranded when exiting the neural tube and entering the domain (left boundary) due to the lack of a chemoattractant gradient. In the leader–follower model, the hypothesis of two cell types results in followers infiltrating the domain despite the absence of a chemoattractant gradient.

Figure 1.2: Leader–follower model of cranial NC cell migration (reproduced from [1]).

(see Figure 1.2b, top).

Although invasion is successful with only leading cells, the cells that exit the neural tube at a later stage lack directional cues because of VEGF depletion. Hence, they crowd the entrance of the pathway and distribute themselves unevenly across the tissue. However, if a follower cell type is introduced that attaches to leading cells, or cells that have made contact with a leading cell, then chains were formed, resulting in coherent cell migration (see Figure 1.2b, bottom).

## 1.2 Outline

As mentioned earlier, the aim of this dissertation is to construct a continuum model that incorporates the leader–follower dynamic, first described in the IBM. In particular, we want to achieve sustained NC cell invasion driven by a combination of a cell-induced gradient and a leader–follower dynamic and understand its mechanics. In the next chapter, we will discuss chemotaxis in general and argue for a cell-induced gradient model of cell migration. Chapter 3 introduces a leader-only model and discusses its potential for travelling wave solutions, but also its limitations. Then, we construct the PDE-based leader–follower model in Chapter 4. In Chapter 5, we show that the leader–follower model can be generalised to an arbitrary number of cell types. Finally, we summarise our work in Chapter 6 and highlight the main conclusions of this dissertation.

# Chapter 2

## Chemotaxis

Chemotaxis is the movement of a cell in response to a chemical gradient. When a cell moves up (down) a positive gradient, the chemical is called a chemoattractant (chemorepellent). It is a process fundamental to the lives of both unicellular and multicellular organisms. Bacteria use chemotaxis to navigate their environment, seeking out nutrients and evading harmful substances. In multicellular organisms, chemotaxis plays many critical roles such as guiding sperm cells to the egg, directing immune cells to inflammation sites, and positioning cells during embryogenesis.

On the population level, chemotaxis is most frequently implemented as an advective flux in a PDE model. Letting  $u(\mathbf{x}, t)$  be the cell density and  $c(\mathbf{x}, t)$  the chemoattractant (or chemorepellent) concentration at position  $\mathbf{x}$  and time  $t$ , the governing equation for  $u$  is

$$\frac{\partial u}{\partial t} = -\nabla \cdot (\mathbf{J}_{\text{diff}} + \mathbf{J}_{\text{chemo}}) , \quad (2.1)$$

where the diffusive flux is  $\mathbf{J}_{\text{diff}} = -D_u \nabla u$  and the chemotactic flux is defined by

$$\mathbf{J}_{\text{chemo}} = u\chi \nabla c . \quad (2.2)$$

Here,  $D_u > 0$  is the diffusion coefficient, assumed constant for simplicity, and  $\chi$  is the chemotactic sensitivity. In general,  $\chi$  is a function that may depend on  $u$  and  $c$ . If  $c$  is a chemoattractant, then  $\chi > 0$  means that the chemotactic flux is directed towards positive gradients of  $c$ . The opposite is true if  $c$  is a chemorepellent. Unless stated otherwise, all chemotactic interactions hereafter are assumed to be attractive.

If  $\chi = k$  with  $k$  constant, it is called the **minimal model** for chemotaxis. Although we will show in Section 2.2 that it is not very useful for describing NC cell migration, it is the simplest possible chemotactic law and can be obtained from other chemotactic laws when taking certain limits in their parameters. The minimal model

thus serves as a reference point throughout this work when analysing other chemotactic models.

Since chemotaxis appears in many forms and shapes, a large variety of chemotaxis models have been constructed to reproduce several pattern forming mechanisms encountered in nature (see [13] for an overview). In our work, we are mainly concerned with signal-dependent sensitivity (SDS) models, where  $\chi$  is a function of  $c$ . We will not derive chemotactic equations from the basic principles of cell motion here, but a review can be found in [14].

In this chapter, first the SDS models used in this work are introduced in Section 2.1. Then, Section 2.2 explores the rationale for a cell-induced gradient model of cell migration, which underlines the need for SDS models.

## 2.1 Signal-Dependent Sensitivity (SDS)

Cells generally perceive molecules in their environment through receptors. These are membrane proteins that bind specific molecules in the exterior of the cell and translate binding events into intracellular signals. Apart from stimulating chemotaxis, these signals may also result in internal changes that modify the cell's behaviour. For instance, if an abundance of a signal is detected, then the cell may respond by increasing or decreasing the number of receptors on its membrane. This explains the need for SDS functions, where the cell responds differently based on the amount of signal present.

An important feature of SDS models is that they can often be represented alternatively by a chemotactic potential  $\phi(c)$  that satisfies

$$\nabla\phi(c) = \chi(c)\nabla c, \quad (2.3)$$

i.e.  $\phi(c)$  is the antiderivative of  $\chi(c)$ . The chemotactic potential thus modifies the signal such that the cells respond directly to the gradient of  $\phi(c)$ :

$$\mathbf{J}_{\text{chemo}} = u\nabla\phi. \quad (2.4)$$

As (2.4) shows, only the gradient of  $\phi(c)$  is relevant and thus for any chemotactic law it is defined up to a constant.

The two most prominent SDS models are the **receptor model** and **logarithmic model** [13], discussed in detail below. They share the property that the chemotactic sensitivity decreases monotonically in  $c$ . This emulates the commonly observed phenomenon of saturation, where increasing the signal results in a decreased response.

Table 2.1: Chemotactic potential  $\phi(c)$  and sensitivity  $\chi(c)$  of chemotaxis models.

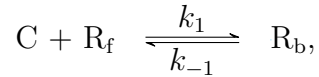
| Name        | $\phi(c)$                | $\chi(c)$                    |
|-------------|--------------------------|------------------------------|
| Minimal     | $kc$                     | $k$                          |
| Receptor    | $k\frac{c}{c+\beta}$     | $k\frac{\beta}{(c+\beta)^2}$ |
| Logarithmic | $k(1+\beta)\ln(c+\beta)$ | $k\frac{1+\beta}{c+\beta}$   |

The receptor model is derived by applying Michaelis–Menten kinetics to receptor binding, while the logarithmic model is based on the phenomenological Weber–Fechner law. The former is the more successful in fitting experimental data and is therefore the more biologically relevant model, while the latter lends itself better to mathematical analysis [13, 15]. Table 2.1 provides an overview of the chemotactic models used in this work.

### 2.1.1 Receptor Model

Cells contain a finite number of receptors on their membrane, and thus their ability to sense chemical signals is limited by the availability of free receptors. Since only bound receptors participate in internal signal transduction, it follows that it is not the signal concentration that is most relevant to cells, but rather the concentration of bound receptors.

Consider the reversible binding between a signal molecule C and a free receptor  $R_f$  to form the bound signal–receptor complex  $R_b$ :



where  $k_1, k_{-1} > 0$  are the binding and unbinding reaction rate constants, respectively. If the binding reaction is governed by second-order kinetics and the unbinding reaction by first-order kinetics, the concentrations of C,  $R_f$  and  $R_b$  are locally governed by

$$\frac{d[C]}{dt} = -k_1[C][R_f] + k_{-1}[R_b], \quad (2.5a)$$

$$\frac{d[R_f]}{dt} = -k_1[C][R_f] + k_{-1}[R_b], \quad (2.5b)$$

$$\frac{d[R_b]}{dt} = +k_1[C][R_f] - k_{-1}[R_b], \quad (2.5c)$$



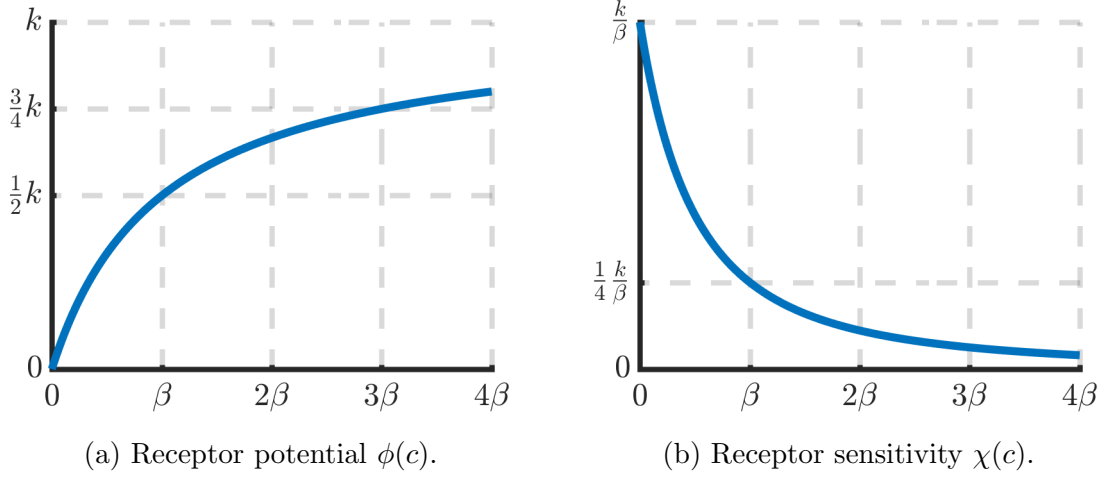


Figure 2.1: Receptor model defined by (2.7) and (2.8).

where  $[\cdot]$  denotes concentration. Assuming that the binding and unbinding reactions take place on a significantly smaller timescale than the chemotactic response, we can impose quasi-steady state conditions. This means that the reactions are locally at equilibrium. Setting all derivatives with respect to time to zero and using the fact that the total concentration of receptors is constant ( $[R_f] + [R_b] = R$ ), we obtain

$$[R_b]_{\text{eq}} = \frac{k_1 R [C]_{\text{eq}}}{k_1 [C]_{\text{eq}} + k_{-1}} = \frac{R [C]_{\text{eq}}}{[C]_{\text{eq}} + K}, \quad K = \frac{k_{-1}}{k_1}, \quad (2.6)$$

where  $[\cdot]_{\text{eq}}$  denotes the equilibrium concentration. This motivates the receptor model with chemotactic potential (plotted in Figure 2.1a)

$$\phi(c) = k \frac{c}{c + \beta} \quad (2.7)$$

and chemotactic sensitivity (plotted in Figure 2.1b)

$$\chi(c) = k \frac{\beta}{(c + \beta)^2}, \quad (2.8)$$

with  $k$  and  $\beta$  positive constants.

In the receptor model, cells respond directly to the concentration of bound receptors. As  $c \rightarrow \infty$ , the chemotactic potential saturates to its maximum value  $k$  and the chemotactic sensitivity vanishes. The parameter  $\beta$  modulates how quickly saturation occurs. The Taylor expansion of (2.8) about  $c = 0$ ,

$$\chi(c) = k \frac{1}{\beta} - 2k \frac{c}{\beta^2} + 3k \frac{c^2}{\beta^3} - \dots = k \sum_{n=0}^{\infty} (-1)^n (n+1) \frac{c^n}{\beta^{n+1}}, \quad (2.9)$$

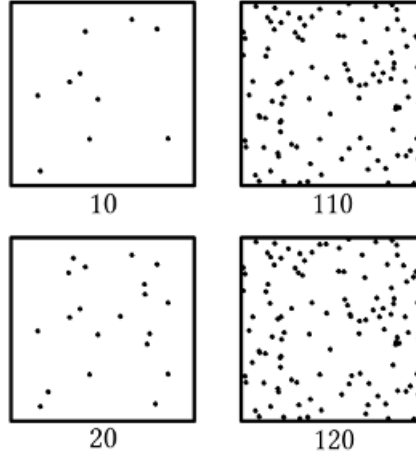


Figure 2.2: Illustration of Weber–Fechner’s law (reproduced from [17]). On both sides, the bottom square contains 10 more dots and than the one above it. However, the increase on the left side is much more noticeable because the change is large compared to the number of dots in the top square.

shows that for low chemoattractant concentrations  $c \ll \beta$ , the chemotactic sensitivity is approximated by the minimal model  $\chi = k/\beta$ . Alternatively, taking the limit  $\beta \rightarrow \infty$  and  $k \rightarrow \infty$  with the ratio  $k/\beta$  constant, the receptor model reduces to the minimal model as well. This would correspond physically to an infinite concentration of receptors, with a constant ratio  $R/K$ .

### 2.1.2 Logarithmic Model

The logarithmic model is derived by applying Weber–Fechner’s law to cell behaviour [16]. This law describes a typical biological response to an external stimulus. It states that the *perceived* change of a stimulus is not proportional to the absolute change of stimulus intensity, but rather the *relative* change. A simple illustration of this law is given by Figure 2.2.

The perceived change in stimulus is what invokes a biological response. Since SDS models can be interpreted as cells responding directly to a gradient in chemotactic potential, as in (2.4), the perceived change corresponds to a change in the chemotactic potential  $\phi$ . The stimulus is the chemoattractant concentration  $c$ , hence

$$d\phi = k \frac{dc}{c}, \quad (2.10)$$

where  $k$  is the proportionality constant. The logarithmic model is thus defined by

$$\phi(c) = k \ln(c), \quad (2.11)$$

$$\chi(c) = \frac{k}{c}. \quad (2.12)$$

This model has been extensively studied because it fits the behaviour of certain bacterial systems [16] and is amenable to travelling wave analysis [15]. Moreover, the chemotactic sensitivity  $\chi(c)$  often needs to be singular in order for travelling wave solutions to exist and (2.12) is the least singular model to satisfy that condition. This is explained further in Chapter 3.

The singular nature of (2.12) is simultaneously the model's downfall [18]. As the chemoattractant concentration approaches zero, the cell velocities induced by chemotaxis far exceed practical limits. Moreover, at low concentrations the stochastic nature of the underlying molecular dynamics introduces increasingly higher levels of noise relative to the signal. It is therefore highly unrealistic to assume that cells are able to precisely sense gradients in  $c$  and maintain a large chemotactic flux.

A modified version of the logarithmic model is given by

$$\phi(c) = k(1 + \beta) \ln(c + \beta), \quad (2.13)$$

$$\chi(c) = k \frac{1 + \beta}{c + \beta}, \quad (2.14)$$

where  $k$  and  $\beta$  are positive constants (functions plotted in Figure 2.3). The original model defined by (2.11) and (2.12) is recovered by setting  $\beta = 0$ . Hereafter, the term “logarithmic” model refers to the model defined by Equations (2.13) and (2.14) and the term “pure” logarithmic model refers to the special case where  $\beta = 0$ .

The factor  $1 + \beta$  was added so that in the limit  $\beta \rightarrow \infty$ , the model reduces to the minimal model with  $\chi = k$  [13]. Similarly as in the receptor model, considering the Taylor expansion of (2.14) about  $c = 0$ ,

$$\chi(c) = \tilde{k} \frac{1}{\beta} - \tilde{k} \frac{c}{\beta^2} + \tilde{k} \frac{c^2}{\beta^3} - \dots = \tilde{k} \sum_{n=0}^{\infty} (-1)^n \frac{c^n}{\beta^{n+1}}, \quad (2.15)$$

where  $\tilde{k} = k(\beta + 1)$ , shows that the logarithmic model is also approximated by the minimal model when  $c \ll \beta$ . For both SDS models, the parameter  $\beta$  modulates the saturating behaviour of the chemotactic sensitivity, thus we will call it the **saturation constant** hereafter.

In addition, comparing (2.8) and (2.14) reveals that a fundamental difference between the receptor and logarithmic model lies in the power of its denominator.

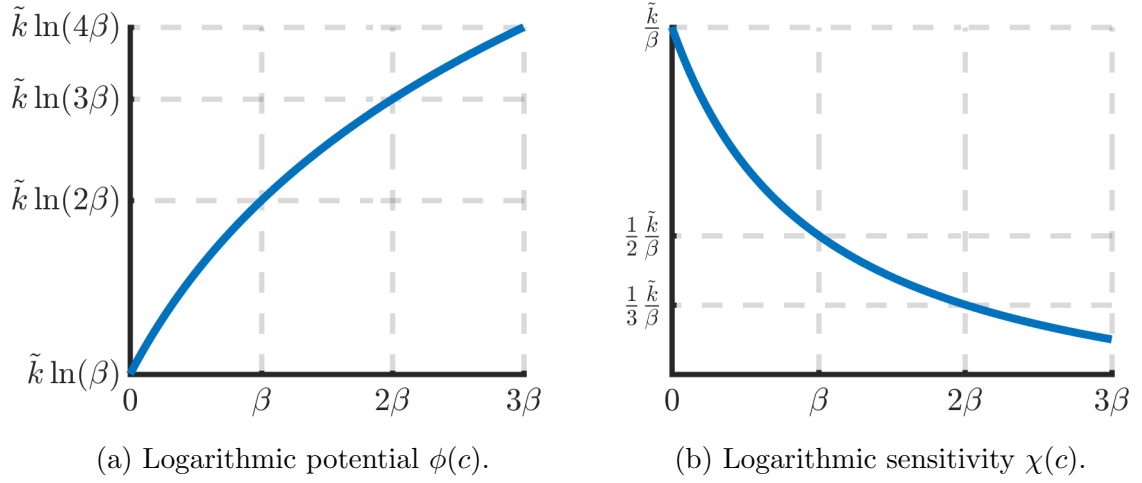


Figure 2.3: Logarithmic law defined by (2.13) and (2.14) with  $\tilde{k} = k(1 + \beta)$ .

As  $c \rightarrow 0$ , the receptor sensitivity grows as  $O(c^{-2})$ , while the logarithmic sensitivity grows as  $O(c^{-1})$ .

## 2.2 Forced Versus Cell-Induced Gradient

Since chemical gradients are the driving force in chemotaxis, a straightforward method to achieve long-distance chemotactic migration would be to simply impose a chemoattractant gradient. Let us consider, by way of illustration, the one-dimensional domain  $[0, L]$ , where the chemoattractant concentration has been fixed at its boundaries and the profile has evolved to a steady state:

$$\begin{cases} \frac{d^2 c}{dx^2} = 0 & x \in [0, L], \end{cases} \quad (2.16a)$$

$$\begin{cases} c = c_0 & x = 0, \end{cases} \quad (2.16b)$$

$$\begin{cases} c = c_L & x = L, \end{cases} \quad (2.16c)$$

where  $c_0$  and  $c_L$  are positive constants such that  $c_0 < c_L$ . The resulting concentration profile is linear in  $x$ ,

$$c(x) = ax + c_0, \quad a = \frac{c_L - c_0}{L}. \quad (2.17)$$

Assuming that the chemotactic sensitivity depends only on  $c$ , we substitute the steady state solution in the governing equation for the cells (2.1) to obtain the advection–diffusion equation

$$\frac{\partial u}{\partial t} + \frac{\partial(uv)}{\partial x} = D_u \frac{\partial^2 u}{\partial x^2}, \quad (2.18)$$

where the advective velocity is given by

$$v(x) = a\chi(ax + c_0), \quad (2.19)$$

for some chemotactic sensitivity function  $\chi(c)$ .

With a forced chemoattractant gradient, the chemotactic sensitivity is completely determined at every position  $x$ . While moving along the domain from  $x = 0$  to  $x = L$ , the cells simultaneously traverse the chemotactic sensitivity from  $\chi(c_0)$  to  $\chi(c_L)$ . Equation (2.19) suggests that SDS models are ill-suited for migration by a forced chemical gradient, as the chemotactic sensitivity declines rapidly along  $x$  so that any attempted invasion quickly grinds to a halt. This is demonstrated in Figures 2.4a and 2.4b. In the minimal model however, the advection velocity is constant ( $v = ak$ ). The resulting cell migration is analogous to a diffusing cell population subject to a uniform flow velocity.

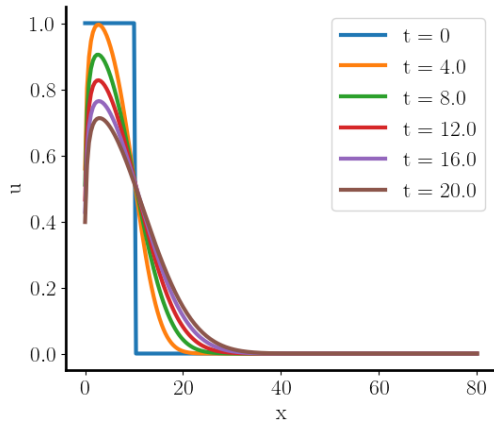
We performed a numerical simulation<sup>1</sup> with a forced gradient for the minimal model and receptor model (details in Figure 2.4c). Equation (2.19) predicts that for the minimal model, the wavespeed is  $v = 2$ , which is verified in Figure 2.4d. On the other hand, Figure 2.4a and Figure 2.4b show that the receptor model fails to achieve persistent migration, as expected.

Even though chemotactic migration under an external chemoattractant gradient is theoretically valid, it represents a highly unrealistic situation when translated to biological situations. Because of the limited number of receptors, cells tend to saturate their chemotactic response at high concentrations of  $c$ . If the chemoattractant concentration varies very little over the migratory domain, then the minimal model is valid as a first-order approximation to the receptor model. However, in this regime the gradients are too shallow for cells to distinguish. For steep gradients on the other hand, cells quickly saturate as they move up the gradient [23].

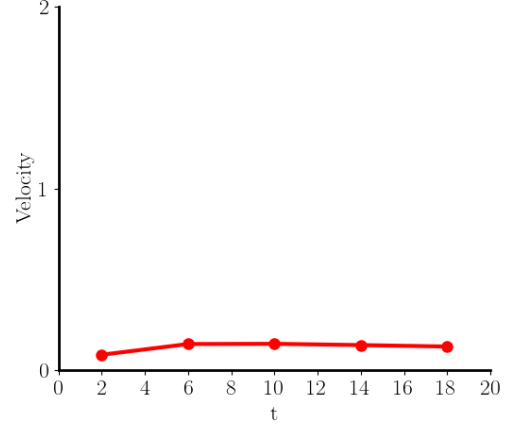
Instead, more sophisticated models of chemotaxis assume that there is some kind of interaction between cells and the chemoattractant that creates the gradient propelling the cells forward. This can be the production of chemoattractant for modelling auto-aggregation phenomena [24, 25], or chemoattractant consumption in long-distance cell migration [1, 2, 15, 23]. Mathematical models of the latter type even allow for travelling wave solutions, as discussed in the next chapter.

---

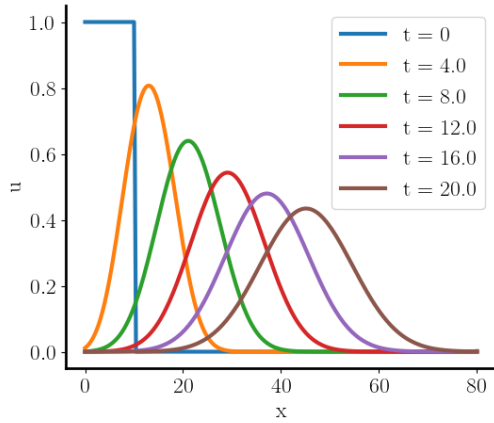
<sup>1</sup>All PDEs in this dissertation were solved numerically by first discretising in time using a Crank–Nicolson scheme, then discretising in space using the finite element method with first-order Lagrange elements [19, 20], and finally implementing the solver in FEniCS through the Python DOLFIN interface [21, 22].



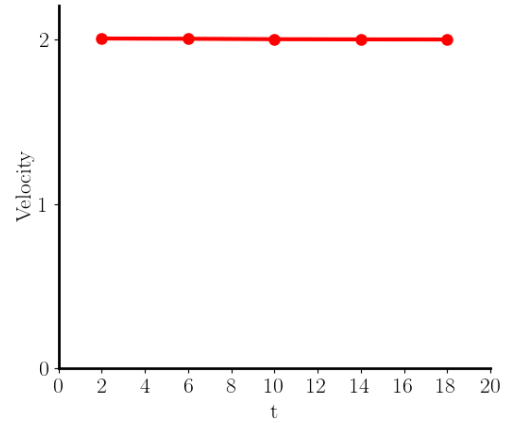
(a) Evolution of concentration profile for receptor model.



(b) Velocity of median point for receptor model.



(c) Evolution of concentration profile for minimal model.



(d) Velocity of median point for minimal model.

Figure 2.4: Numerical results of forced chemoattractant gradient applied to minimal and receptor chemotaxis model. Equation (2.18) was solved on the domain  $[0, L]$  for  $t \in [0, T]$ . Parameter values are given in Table A.1. The median point at time  $t$  was defined as the point that divides the domain into two intervals that cover the domain and evenly split the total cell mass, i.e the point  $\hat{x} \in [0, L]$  that satisfies  $\int_0^{\hat{x}} u \, dx = \int_{\hat{x}}^L u \, dx$ . Zero-flux boundary conditions were used and initial conditions were  $u_0(x) = 1 - H(x - 10)$  with  $H$  the Heaviside step function.

# Chapter 3

## Leader Model

The classical Keller–Segel model for chemotaxis couples the evolution of the chemoattractant with that of the cells by assuming that the cells can produce or consume the chemoattractant [13]. The result is a coupled advection–diffusion–reaction PDE system,

$$\frac{\partial u}{\partial t} = -\nabla \cdot (u\chi(c)\nabla c - D_u\nabla u) , \quad (3.1a)$$

$$\frac{\partial c}{\partial t} = D_c\nabla^2 c + f(u, c) , \quad (3.1b)$$

where  $D_c$  is the chemoattractant diffusion coefficient and  $f(u, c)$  is the net production of  $c$ .

In this chapter, we focus on a one-dimensional Keller–Segel model for a NC cell population consisting only of leader cells moving up a cell-induced chemoattractant gradient, governed by some yet to be determined chemotactic law and second-order chemoattractant consumption:

$$\frac{\partial u}{\partial t} = -\frac{\partial}{\partial x} \left( u\chi(c)\frac{\partial c}{\partial x} - D_u\frac{\partial u}{\partial x} \right) , \quad (3.2a)$$

$$\frac{\partial c}{\partial t} = D_c\frac{\partial^2 c}{\partial x^2} - \alpha uc , \quad (3.2b)$$

where  $\alpha > 0$  is the consumption constant. We want to study the potential of this model for persistent cell invasion on an unbounded domain. The system (3.2) is invariant under the coordinate transformation  $x \rightarrow -x$ , hence without loss of generality we consider only cell invasion along the positive  $x$ -direction. We assume that the cells consume the chemoattractant completely as they migrate, hence at the boundaries

we impose

$$u(-\infty, t) = u_-, \quad u(\infty, t) = 0, \quad (3.3a)$$

$$c(-\infty, t) = 0, \quad c(\infty, t) = c_+, \quad (3.3b)$$

where  $u_-, c_+ > 0$  are constants. The initial conditions are

$$u(x, t = 0) = u_0(x), \quad (3.4a)$$

$$c(x, t = 0) = c_0(x), \quad (3.4b)$$

where  $u_0$  and  $c_0$  satisfy the boundary conditions (3.3).

Interestingly, (3.2) is capable of supporting travelling wave solutions [15]. These are defined as wave solutions that propagate at a constant velocity and maintain a fixed shape [5]. On a one-dimensional domain, this is expressed as

$$u(x, t) = U(z), \quad c(x, t) = C(z), \quad z = x - vt, \quad (3.5)$$

where  $v$  is the wavespeed. We assume  $v > 0$  since we are considering movement along the positive  $x$ -direction and  $v = 0$  corresponds to a stationary wave, as opposed to a travelling wave. This type of solution is particularly interesting in the context of cell invasion, as it describes the directed movement of a cell population over arbitrary long distances.

The existence of travelling wave solutions seems to suggest that long-distance cell migration is a solved problem and that the efforts that went into this dissertation were better spent elsewhere. However, there is a fundamental mismatch between the mathematical existence of travelling waves in Keller–Segel models and the biological reality of cell invasion, which is related to the condition that the chemotaxis law is singular. This is proven in Section 3.1 and discussed further in Section 3.3. Despite this inherent limitation, we will perform a travelling wave analysis of (3.2) in Section 3.2 to understand long-distance cell migration in mathematically ideal conditions. This will help us understand certain aspects of chemotaxis in biologically relevant systems, which we will discuss in Section 3.3. For Sections 3.1 and 3.2, we follow the argument presented in [15].



### 3.1 Necessity of Singular Chemotaxis

Substituting the travelling wave assumption (3.5) in (3.2) yields a system of nonlinear ODEs,

$$-vU' = -(U\chi(C)C' - D_u U')', \quad (3.6a)$$

$$-vC' = D_c C'' - \alpha UC, \quad (3.6b)$$

where the prime symbol denotes differentiation with respect to  $z$ . By inserting the travelling wave assumption, we lose the ability to solve for arbitrary initial conditions, as only initial conditions that are compatible with travelling wave solutions are permitted. The boundary conditions, however, are still important:

$$U(-\infty) = u_-, \quad C(-\infty) = 0, \quad U(\infty) = 0, \quad C(\infty) = c_+. \quad (3.7)$$

It follows from these boundary conditions that the first derivatives of  $U$  and  $C$  vanish as  $z \rightarrow \pm\infty$ . Otherwise, their absolute values would grow unboundedly at the boundaries.

Rewriting (3.6a) as

$$(D_u U' + vU - U\chi(C)C')' = 0, \quad (3.8)$$

shows us that the expression inside the brackets is equal to a constant,

$$D_u U' + vU - U\chi(C)C' = A_0. \quad (3.9)$$

We evaluate (3.9) at  $z \rightarrow \infty$  to conclude that  $A_0$  must be zero because of the boundary conditions (3.7). We then divide by  $U$  and integrate from  $\tilde{z} = 0$  to  $\tilde{z} = z$ ,

$$U(z) = u_0 \exp \left( -\frac{v}{D_u} z + \frac{1}{D_u} \int_0^z \chi(C)C' d\tilde{z} \right), \quad (3.10)$$

where  $u_0 = U(0) \geq 0$  (negative densities or concentrations are physically meaningless in this context). The integral inside the exponent is written alternatively as

$$\int_0^z \chi(C) \frac{dC}{d\xi} d\xi = \int_{c_0}^{C(z)} \chi(\tilde{C}) d\tilde{C}, \quad (3.11)$$

where  $c_0 = C(0) \geq 0$ . We assume that  $\chi(c)$  has no singularities for  $c \geq 0$ . Then the absolute value of (3.11) as  $z \rightarrow -\infty$  is bounded by some constant  $K$ ,

$$\left| \int_{c_0}^{C(-\infty)} \chi(\tilde{C}) d\tilde{C} \right| = \left| \int_{c_0}^0 \chi(\tilde{C}) d\tilde{C} \right| \leq K \quad (3.12)$$

where we used the boundary condition  $C(-\infty) = 0$ .

In order for  $U(z)$  to be finite as  $z \rightarrow -\infty$ , the argument of the exponential function in (3.10) must be bounded above. Since we showed that the integral in (3.10) is bounded as  $z \rightarrow -\infty$ , this cannot be the case. Therefore we have reached a contradiction and  $\chi(c)$  must contain a singularity for  $c \geq 0$ .

Furthermore, the singularity in  $\chi(c)$  must occur at  $c = 0$  to avoid that (3.6a) is ill-defined for some finite  $z$ . The expression  $\chi(C(z))C'(z)$  does not necessarily blow up as  $z \rightarrow -\infty$  since  $C'(-\infty) = 0$ , therefore (3.6a) can still be well-defined. In fact, evaluating (3.9) in the limit  $z \rightarrow -\infty$ ,

$$u_- (v - \chi(C(-\infty))C'(-\infty)) = 0, \quad (3.13)$$

shows that  $\chi(C(-\infty))C'(-\infty)$  is equal to the constant value  $v > 0$ , which it could not be if  $\chi(c)$  had no singularity at  $c = 0$ .

We can make a stronger statement about the singularity of  $\chi(c)$ . Assuming that  $\chi(c)$  is of the form  $c^{-a}$ , with  $a$  a non-negative constant, we see that the integral

$$\int_{c_0}^0 \frac{dc}{c^a} = \lim_{\tilde{c} \rightarrow 0} \begin{cases} \frac{1}{1-a} [c^{1-a}]_{c_0}^{\tilde{c}} & \text{for } a \neq 1 \\ [\ln(c)]_{c_0}^{\tilde{c}} & \text{for } a = 1 \end{cases} \quad (3.14)$$

converges for  $a < 1$ . In conclusion, if  $\chi(c)$  has a single singularity at  $c = 0$ , then  $\chi(c)$  needs to be at least as singular as  $c^{-a}$  with  $a \geq 1$  as  $c \rightarrow 0$  for finite travelling wave solutions to exist. The least singular form that satisfies this condition is  $a = 1$ , which is exactly the pure logarithmic model. In the next section we will prove that the pure logarithmic model indeed allows such solutions.

## 3.2 Travelling Wave Analysis

Repeating the first steps of Section 3.1 with the pure logarithmic chemotaxis law yields the following expression for  $U(z)$ ,

$$U(z) = Qe^{-(v/D_u)z} C^{k/D_u}(z), \quad (3.15)$$

with constant  $Q$  derived from the integration constant. Substituting in (3.6b) and rearranging, we obtain

$$D_c C'' + vC' - \alpha Q e^{-pz} C^r = 0, \quad (3.16)$$

with  $r = k/D_u + 1$  and  $p = v/D_u$ . If  $C(z)$  is a solution to (3.16), then the translated solution  $C(z + \Delta z)$  satisfies (3.16) with  $Q^* = Q \exp(-p\Delta z)$  in the place of  $Q$ . This

shows that changing the value of  $Q$  is equivalent to translating the travelling wave solution, hence the choice of  $Q$  is arbitrary. For simplicity, we choose  $Q = 1$ .

We can eliminate the variable coefficient  $\exp(-pz)$  in (3.16) by transforming the dependent variable [15]. Letting

$$\mu = -\frac{p}{r-1} = -\frac{v}{k}, \quad (3.17)$$

we define the transformation

$$C(z) = W(z)e^{-\mu z}, \quad (3.18)$$

so that

$$C^r e^{-pz} = W^r e^{-\mu z}, \quad (3.19)$$

$$C' = (W' - \mu W) e^{-\mu z}, \quad (3.20)$$

$$C'' = (W'' - 2\mu W' + \mu^2 W) e^{-\mu z}. \quad (3.21)$$

Substituting and dividing through by  $\exp(-\mu z)$ , Equation (3.16) is rewritten as

$$D_c W'' + s W' + f(W) = 0, \quad (3.22)$$

with

$$s = v - 2D_c \mu = v \left[ 1 + 2\frac{D_c}{k} \right] > 0, \quad (3.23)$$

and

$$f(W) = \eta W \left[ 1 - \frac{\alpha}{\eta} W^{r-1} \right], \quad (3.24)$$

$$\eta = D_c \mu^2 - v \mu = \frac{v^2}{k^2} (D_c + k) > 0. \quad (3.25)$$

Inspection of (3.22) reveals that it is analogous to a Fisher travelling wave equation for the transformed variable  $W$  with wavespeed  $s$ . The equivalent system of ODEs is

$$\begin{cases} \frac{dW}{dz} = \xi, \end{cases} \quad (3.26a)$$

$$\begin{cases} \frac{d\xi}{dz} = -\frac{s}{D_c} \xi - \frac{\eta}{D_c} W \left[ 1 - \frac{\alpha}{\eta} W^{r-1} \right]. \end{cases} \quad (3.26b)$$

This system was analysed in [26] for  $\alpha = \eta$  and  $r = 2$  to prove the existence and uniqueness of travelling wave solutions. An analogous analysis can be carried out for  $r > 1$  and arbitrary  $\alpha > 0$ , provided  $s, \eta, D_c > 0$ , but for brevity we will omit the proofs and directly use the main results of the Fisher wave analysis.

The fixed points and corresponding eigenvalues of (3.26) are

$$(W_1, \xi_1) = (0, 0) \quad : \quad \lambda_1^\pm = \frac{-s \pm \sqrt{s^2 - s_{\min}^2}}{2D_c}, \quad (3.27a)$$

$$(W_2, \xi_2) = \left( \left( \frac{\eta}{\alpha} \right)^{D_u/k}, 0 \right) \quad : \quad \lambda_2^\pm = \frac{-s \pm \sqrt{s^2 + s_{\min}^2}}{2D_c}, \quad (3.27b)$$

with  $s_{\min} = 2\sqrt{D_c\eta}$ . The condition for non-negative solutions is

$$s \geq s_{\min} = 2\sqrt{D_c\eta}, \quad (3.28)$$

or in terms of the original chemotaxis parameters,

$$v \left[ 1 + 2\frac{D_c}{k} \right] \geq 2\sqrt{D_c \frac{v^2}{k^2} (D_c + k)}. \quad (3.29)$$

The wavespeed  $v$  is thus bounded below by

$$v \geq v_{\min} = 0. \quad (3.30)$$

However, as stated earlier, we assume that  $v > 0$ . This implies that  $s > s_{\min}$ , so that the fixed points (3.27) each have two distinct eigenvalues.

The solution of  $W(z)$  as  $z \rightarrow -\infty$  is then given by

$$W(z) \sim \left( \frac{\eta}{\alpha} \right)^{D_u/k} + Ae^{\lambda_2^+ z} \text{ as } z \rightarrow -\infty, \quad (3.31)$$

with  $A$  some non-negative constant. Reverting back to the original dependent variable  $C(z)$  using (3.18),

$$C(z) \sim \left[ \left( \frac{\eta}{\alpha} \right)^{D_u/k} + Ae^{\lambda_2^+ z} \right] e^{-\mu z} \text{ as } z \rightarrow -\infty. \quad (3.32)$$

Finally, using Equation (3.15),

$$U(z) \sim \left[ \left( \frac{\eta}{\alpha} \right)^{D_u/k} + Ae^{\lambda_2^+ z} \right]^{k/D_u} \text{ as } z \rightarrow -\infty. \quad (3.33)$$

In order to satisfy the boundary condition  $U(-\infty) = u_-$ , we thus need

$$\frac{\eta}{\alpha} = u_-, \quad (3.34)$$

which yields an exact expression for the wavespeed after substituting (3.25),

$$v = k \sqrt{\frac{\alpha u_-}{D_c + k}}. \quad (3.35)$$

### 3.3 Discussion

The above analysis is for an unbounded domain, so we checked whether (3.2) gives rise to travelling waves on a finite domain  $[0, L]$  by solving the equations numerically. The initial conditions were

$$u_0(x) = 0, \quad (3.36a)$$

$$c_0(x) = c_+. \quad (3.36b)$$

This represents a domain with an initial uniform concentration of chemoattractant and without any cells. The cells are introduced by imposing the boundary condition<sup>1</sup>

$$u = u_- \quad \text{at } x = 0. \quad (3.37)$$

For the chemoattractant however, we cannot simply impose  $c = 0$  at the boundary because that renders the PDE ill-posed because of the singularity in  $\chi(c)$  at  $c = 0$ . We therefore apply zero-flux boundary conditions,

$$\frac{\partial c}{\partial x} = 0 \quad \text{at } x = 0. \quad (3.38)$$

And similarly at  $x = L$ ,

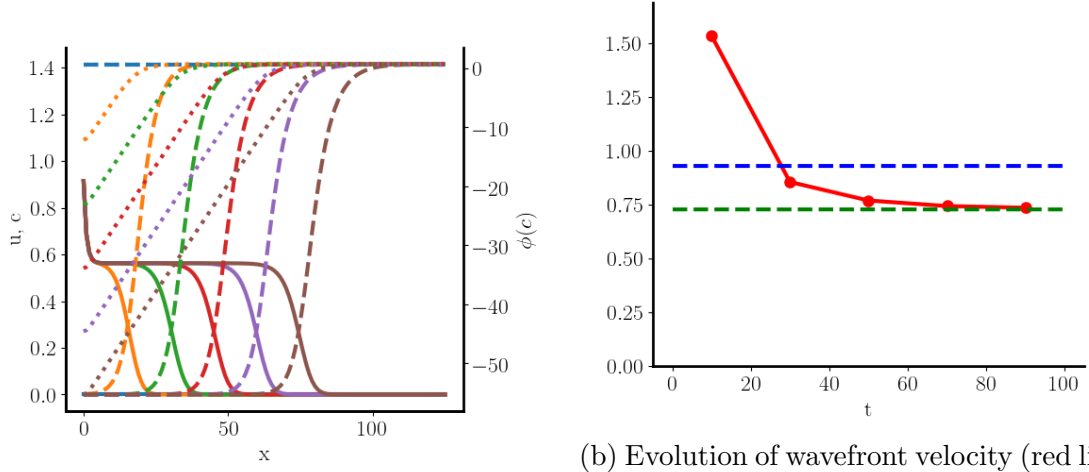
$$\frac{\partial c}{\partial x} = \frac{\partial u}{\partial x} = 0 \quad \text{at } x = L. \quad (3.39)$$

Since the chemotactic flux of  $u$  is proportional to  $\partial c / \partial x$ , the conditions (3.39) taken together ensure that both the chemotactic and diffusive flux of  $u$  vanish, resulting in a zero total flux. We thus assume that the cells enter at  $x = 0$ , but that no cells pass through the boundary at  $x = L$ . We also assume that the chemoattractant passes through neither of the boundaries.

The results of the numerical simulation are somewhat unexpected (see Figure 3.1a). First of all, the cell density initially drops very steeply, before stabilising to a flat profile at a lower density than the boundary value  $u_-$ . This plateau value increases when imposing a higher boundary value, but the difference is not fixed (numerical results omitted for brevity). Secondly, although the cell profile does acquire a constant shape and velocity away from the boundary, the wavespeed is lower than (3.35) predicts, as

---

<sup>1</sup>Although the boundary condition (3.37) is incompatible with the initial condition (3.36a), the literature on error analysis for mixed finite element methods applied to parabolic problems indicates that numerical methods are generally well-behaved despite non-smooth or incompatible initial data [27, 28, 29]. Therefore, we will not discuss any theoretical considerations related to incompatible or non-smooth initial data.



(a) Evolution of profiles. Solid, dashed and dotted lines correspond to  $u$ ,  $c$  and  $\phi(c)$  respectively. Results are plotted at regular intervals of 20 time units.

(b) Evolution of wavefront velocity (red line). The dashed blue line indicates the expected wavespeed of  $2/\sqrt{3} \approx 1.15$ , while the green line indicates the expected wavespeed using the observed plateau cell density instead of  $u_-$ .

Figure 3.1: Numerical results for leader model with naive boundary conditions. Equation (3.2) was solved on the domain  $[0, L]$  for  $t \in [0, T]$ . Parameter values are given in Table A.2. See text for details on boundary conditions and initial conditions.

Figure 3.1b shows. Presumably, this difference is caused by the density drop near the boundary, which results in a travelling wave with a lower cell density. Indeed, when inserting the plateau value of  $u$  in the wavespeed expression, we see that it matches the observed wavespeed, also shown on Figure 3.1b.

The question is then, what causes the sudden drop in cell density at the boundary? To better understand the role of chemotaxis in this system, we plotted the chemotactic potential  $\phi(c) = k \ln(c)$  as a dotted line in Figure 3.1b. Although the chemoattractant profile behind the wavefront appears flat, plotting the chemotactic potential shows that the concentration decays at an exponential rate towards the boundary, resulting in a linear profile for the chemotactic potential. This induces a constant advective velocity due to chemotaxis, as predicted by Equation (2.4). This is similar to the response of the minimal model to a linear chemoattractant profile, described in Section 2.2. Meanwhile, the profile of  $u$  is similarly flat behind the wavefront. The diffusive flux of  $u$  depends linearly on the gradient of  $u$ , making its contribution negligible here.

Near the boundary  $x = 0$  however, the zero-flux boundary conditions force the profile of  $c$  to be flat. Hence, the chemoattractant gradient required for a uniform chemotactic velocity can locally not be created. As a result, there is a narrow region near the boundary where cell transport is dominated by diffusion. At a certain distance from the boundary, the chemoattractant profile stabilises into an exponential form and the cells start moving uniformly. The sharp drop in  $u$  thus occurs in between cells entering the boundary and cells participating in uniform chemotactic transport.

In order to reproduce the travelling wave solution on a finite domain without a drop in  $u$ , we thus need to ensure that the boundary conditions at  $x = 0$  for  $u$  and  $c$  are compatible. In particular, the gradient of  $\phi(c)$  must induce a chemotactic flux equivalent to an advective flux with the travelling wave velocity  $v$ . Concretely,

$$J_{\text{chemo}} = u \frac{\partial \phi(c)}{\partial x} = uv \quad \text{at } x = 0. \quad (3.40)$$

Substituting  $\phi(c) = k \ln(c)$  and dividing by  $u$  yields

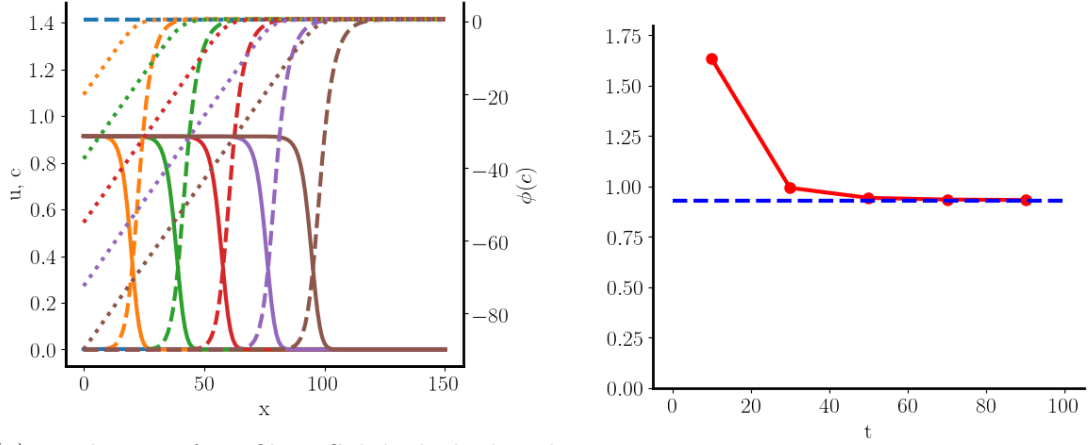
$$\frac{k}{c} \frac{\partial c}{\partial x} = v \quad \text{at } x = 0. \quad (3.41)$$

This corresponds exactly to the condition imposed on  $\chi(C(-\infty))C'(-\infty)$  for the travelling wave system by (3.13) in Section 3.1. As  $z \rightarrow -\infty$ , the chemotactic flux in the travelling wave system must be such that the cells advect at the constant travelling wave velocity  $v$ . Since the cell profile is very quickly dominated by the chemotactic flux behind the wavefront, the boundary  $x = 0$  on the finite domain can be considered sufficiently far away such that we may impose (3.41). We thus obtain a Robin boundary condition for  $c$ :

$$k \frac{\partial c}{\partial x} - vc = 0 \quad \text{at } x = 0. \quad (3.42)$$

With the Robin boundary condition in place instead the zero-flux boundary condition, the cell profile does not drop at the boundary and the observed wavespeed matches exactly the predicted wavespeed (see Figure 3.2). Our numerical simulations therefore confirm the analytical results of the travelling wave analysis. We now proceed to analysing the influence of model parameters on the wavespeed.

Intuitively, we would expect cells to migrate faster for a larger chemotactic sensitivity coefficient  $k$ . This is indeed the case, as (3.35) shows. Moreover, an increased consumption constant  $\alpha$ , or asymptotic cell density  $u_-$ , results in a higher wavespeed as well. These two factors are related, since the consumption of  $c$  in (3.2b) is governed by  $\alpha u$ . The effect of  $u$  is scaled by  $\alpha$ , with  $\alpha u$  representing the overall consumption rate.



(a) Evolution of profiles. Solid, dashed and dotted lines correspond to  $u$ ,  $c$  and  $k\phi(c)$  respectively. Results are plotted at regular intervals of 20 time units.

(b) Evolution of wavefront velocity. The dashed blue line indicates the expected wavespeed of  $2/\sqrt{3} \approx 1.15$ .

Figure 3.2: Numerical results for leader model with Robin boundary conditions for  $c$ . Except for the boundary condition (3.42), all parameters and conditions are identical to the ones used in Figure 3.1.

By definition, the effect of diffusion is to diminish gradients. Therefore, a higher chemoattractant diffusion coefficient should reduce the gradient sensed by the cells, resulting in a lower chemotactic flux. This explains why the wavespeed is a decreasing function in  $D_c$ .

We can interpret the chemotaxis wavespeed in an alternative way by considering the special case  $D_c = 0$ . It can be shown that the wavespeed is then [15]

$$v = \sqrt{k\alpha u_-}. \quad (3.43)$$

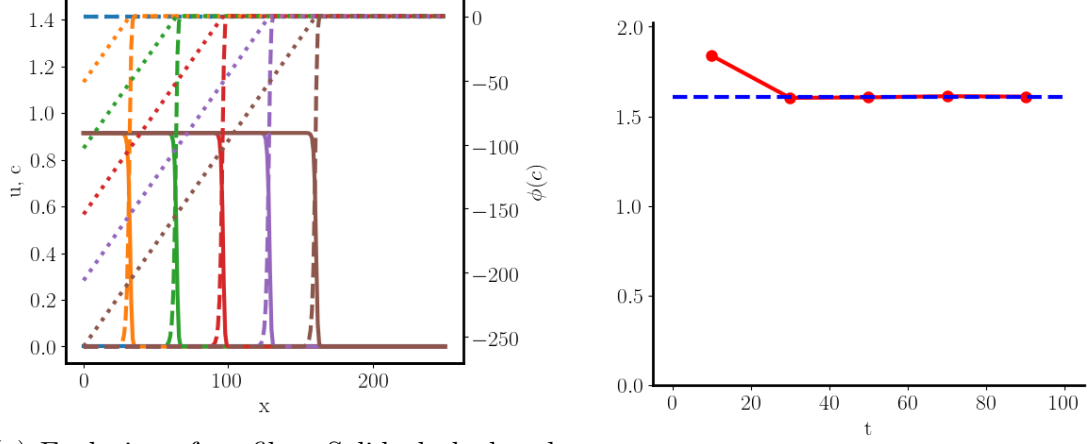
This is the same as the wavespeed obtained before when setting  $D_c = 0$ . Thus, the expression (3.35) is valid for  $D_c \geq 0$ . The profile is qualitatively similar to Figure 3.2a, but with a steeper profile for  $u$  and  $c$  (see Figure 3.3a)<sup>2</sup>

Behind the wavefront, we see that  $u \approx u_-$ . Consider the travelling wave equation with  $U(z)$  approximately constant with value  $u_-$ . We have for  $C$

$$-vC' \approx -\alpha u_- C, \quad (3.44)$$

<sup>2</sup> We did not apply any boundary conditions on  $c$  in this simulation because with  $D_c = 0$ , there are no spatial derivatives in the governing equation for  $c$ .





(a) Evolution of profiles. Solid, dashed and dotted lines correspond to  $u$ ,  $c$  and  $k\phi(c)$  respectively. Results are plotted at regular intervals of 12 time units.

(b) Evolution of wavefront velocity (red line). The dashed blue line indicates the expected wavespeed of 2.

Figure 3.3: Numerical results for leader model with  $D_c = 0$ . Except for  $D_c = 0$ ,  $L = 250$ , all parameters are identical to the ones used in Figure 3.2.

i.e.  $C(z)$  is an exponential function of  $z$  with growth rate  $\alpha u_-/v$ . The cell diffusion is negligible in this regime, hence for  $U$  with  $\chi(c) = kc^{-1}$ ,

$$-vU' \approx -(UkC^{-1}C')' = -\frac{k\alpha u_-}{v}U', \quad (3.45)$$

where (3.44) was substituted in the last equality. Assuming  $U'$  is small but non-zero, we divide through by  $U'$  and rearrange to get

$$v^2 = k\alpha u_-, \quad (3.46)$$

which corresponds to (3.43).

In summary, the consumption behind the wavefront, given by  $\alpha u_-$ , creates an exponential profile for  $c$  with growth rate  $\alpha u_-/v$ . Simultaneously, this causes the cells to move at the advective velocity  $k\alpha u_-/v$ , which must equal the travelling wave velocity  $v$ . The effect of chemoattractant diffusion can then be interpreted as perturbing the exponential growth rate of  $c$  by a saturating factor  $k/(D_c + k)$ , so that

$$v^2 = k\alpha u_- \frac{k}{D_c + k}. \quad (3.47)$$

In either case, this illustrates that in the leader model, migration is governed by the *creation* and *pursuit* of a chemoattractant gradient. The creation of the chemoattractant gradient is initiated by the overall consumption rate  $\alpha u_-$  and diminished by

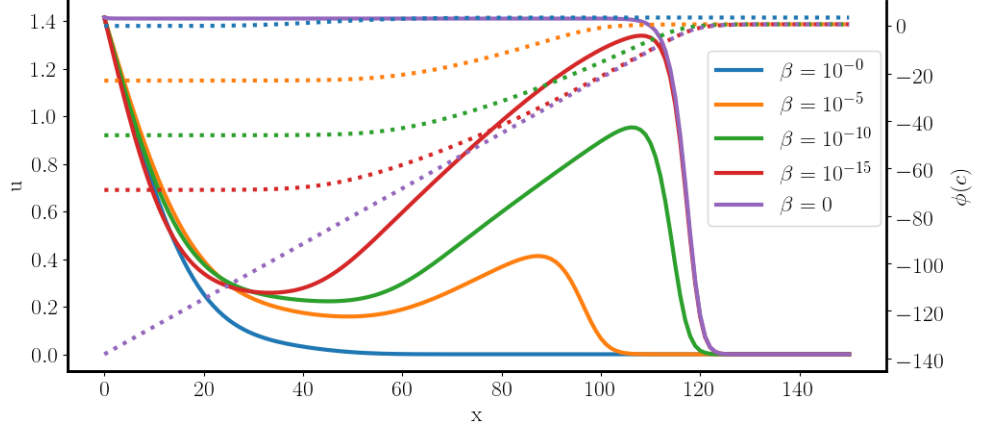


Figure 3.4: Profiles of  $u$  (solid lines) and  $\phi(c)$  (dotted lines) at  $t = 100$  for leader model with  $\beta > 0$ . Other parameters and conditions were the same as in Figure 3.2.

diffusion, as represented by  $k/(D_c + k)$ . The pursuit is determined by the chemotactic law, fixed to the pure logarithmic law here, and the chemotactic coefficient  $k$ .

### 3.4 Failure of Non-Singular Chemotaxis

We have shown that persistent cell migration over arbitrary distances is possible when the chemotaxis law is singular. However, as discussed in Section 2.1.2, a singular chemotactic law is hard to justify from a biological point of view. Instead, we need to assume that cells cannot become infinitely sensitive to chemotactic gradients as  $c \rightarrow 0$ . In the context of logarithmic chemotaxis, this means that  $\beta > 0$ . On the other hand, we have proven in Section 3.1 that travelling wave solutions cannot exist in Keller–Segel models with non-singular chemotaxis. To demonstrate this, we ran simulations similar to Figure 3.2, but with different values of  $\beta$  and plotted the results in Figure 3.4.

Except for when  $\beta = 0$ , we see that the chemotactic potential reaches a plateau value behind the wavefront. This precludes any chemotactic activity between the boundary  $x = 0$  and the wavefront, creating a gap where cell motion is dominated by diffusion. As the wavefront progresses, it gradually loses cells due to diffusion so that its invasion speed and peak cell density decays over time.

A similar phenomenon occurs when the receptor model is simulated for different  $\beta$  (Figure 3.5). However, in this case the chemotactic potential is constrained between 0 and  $k$  due to the saturating property of the receptor model. Only when the concen-

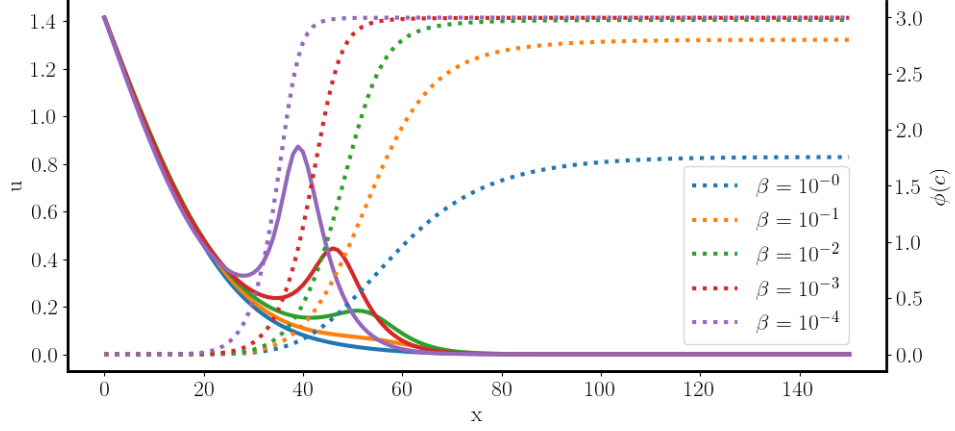


Figure 3.5: Profiles of  $u$  (solid lines) and  $\phi(c)$  (dotted lines) at  $t = 200$  with receptor model for different  $\beta$ . Except for  $k = 3$  and zero-flux boundary conditions for  $c$  at  $x = 0$ , the remaining parameters and conditions were the same as in Figure 3.2.

tration  $c$  reaches values comparable to  $\beta$  will a gradient in the potential appear. This has the consequence that the chemotactically active cells are confined to a narrow interval. An additional consequence of this is that there exists a lag period for small  $\beta$  where chemotactic activity is non-existent because the lowest value of  $c$  is still much higher than  $\beta$ . The narrow peak and lag period are both properties that have been observed experimentally [23].

For either chemotaxis law, the non-singular nature of the chemotactic sensitivity function means that they cannot generate cell migration over arbitrary long distances. This is because for  $c < \beta$ , both chemotaxis models approach the minimal model while simultaneously only perceiving shallow gradients. For some biological systems, cells only need to bridge a small distance and thus the leader model discussed here is sufficient [23]. In other cases, it can be argued that the Keller–Segel model overlooks certain aspects of individual cell behaviour that are crucial to migration. Therefore, an alternative modelling approach to chemotaxis involves explicitly describing individual cell behaviour, such as the IBM model introduced in Chapter 1. In the next chapter, a different model of chemotaxis is proposed that strikes a balance between treating the cells as a single, homogeneous population and treating each cell as an individual.

# Chapter 4

## Leader–Follower Model

As we saw in the previous chapter, a biologically realistic Keller–Segel model with non-singular chemotaxis results in a chemotactic wavefront that decays over time. This phenomenon also occurs in individual-based models and has been observed experimentally [23]. The fundamental issue is a lack of chemotactic activity behind the wavefront, caused by a shallow gradient and a lower bound on the chemotactic sensitivity. In the leader–follower IBM model, this hurdle was overcome by introducing a distinct cell subpopulation that took directional cues from other cells instead of the chemoattractant [1, 2].

In this chapter, we construct and analyse a continuum model inspired by the leader–follower dynamics of the IBM model. For this purpose, we first introduce a follower cell type that trails leader cells by directly sensing gradients in the leader density. However, we show in Section 4.1 that such a model falls short and an additional interaction between leaders and followers is required. Section 4.2 extends the model with terms that model cell differentiation, which greatly improve the quality and robustness of the leader–follower model. We also explore the potential of the extended model for self-organisation and the impact of different chemotactic models. Finally, we conclude with a discussion in Section 4.4.

We extend the leader model from Chapter 3 by introducing an additional cell type,

denoted by  $v(\mathbf{x}, t)$ , that is attracted to the leader cell type in a cytotoxic fashion<sup>1</sup>:

$$\frac{\partial u}{\partial t} = -\nabla \cdot (u\chi_u(c)\nabla c - D_u\nabla u) \quad (4.1a)$$

$$\frac{\partial v}{\partial t} = -\nabla \cdot (v\chi_v(u)\nabla u - D_v\nabla v) \quad (4.1b)$$

$$\frac{\partial c}{\partial t} = D_c\nabla^2 c - \alpha(u + v)c, \quad (4.1c)$$

where  $\chi_v(u)$  is the cytotoxic sensitivity and  $D_v$  is the follower diffusion coefficient, assumed to be constant. We call  $v$  the **follower** cell type because they follow the leader cell type by cytotoxic. This models a local interaction where followers attach to leaders by cell to cell contact. In the next chapter, we will discuss a leader–follower model where the interaction takes place through chemicals, so to distinguish these models we will refer to the current model as the **direct** leader–follower model. Unless stated otherwise, we use the logarithmic chemotaxis law for  $\chi_u(c)$  and  $\chi_v(u)$ , with corresponding chemotactic coefficients  $k_u, k_v$  and saturation constants  $\beta_u, \beta_v$ . Also, we assume that the follower cells consume the chemoattractant in a similar fashion to the leaders.

## 4.1 Failure of Fixed Subpopulations

To quantify whether the direct leader–follower model (4.1) has any impact on the amount of invasion, we conducted a numerical experiment similar to one of the experiments devised for the IBM model [1]. We start out on the one-dimensional domain  $[0, 175]$  with a uniform chemoattractant concentration and no cells,

$$u(x) = v(x) = 0, \quad c(x) = 1 \quad \text{at } t = 0. \quad (4.2)$$

For  $t \in (0, 100]$ , cells enter from the neural crest at the boundary  $x = 0$ , but only when the total cell density  $u + v$  at the boundary is below the maximum cell density  $n_{\max}$ . This simulates the effect of cells crowding the neural crest and blocking new cells from entering the domain. In addition, we want to control the number of leaders and followers that are injected into the system. Thus, given some fraction  $\sigma \in [0, 1]$ , only leader cells enter for  $t \in (0, \sigma \times 100]$ , followed by a stream exclusively consisting of follower cells for  $t \in (\sigma \times 100, 100]$ .

---

<sup>1</sup>In analogy with chemotaxis, which is movement caused by a chemical gradient, cytotoxic is movement caused by a cell gradient.

First, we define a non-crowding cell flux  $J_{\text{in}}(u, v)$  that is positive for  $u + v < n_{\text{max}}$  and zero otherwise. In order to smooth out the transition, we use the approximation

$$H_b(x) = \frac{1}{2} + \frac{1}{2} \tanh(bx), \quad (4.3)$$

where the parameter  $b$  modulates the steepness of  $H_b(x)$ . The higher the value of  $b$ , the more abrupt the transition is in  $H_b(x)$  from 0 to 1 about  $x = 0$ . The non-crowding cell flux was thus defined by

$$J_{\text{in}}(u, v) = g(1 - H_b(u + v - n_{\text{max}})), \quad (4.4)$$

where  $g > 0$  is the constant base cell flux.

The two stages of cell entry were then implemented by imposing the boundary conditions

$$J_u = J_{\text{in}}(u, v), \quad J_v = 0, \quad \text{at } x = 0, \text{ for } t \in (0, \sigma \times 100], \quad (4.5)$$

$$J_u = 0, \quad J_v = J_{\text{in}}(u, v), \quad \text{at } x = 0, \text{ for } t \in (\sigma \times 100, 100], \quad (4.6)$$

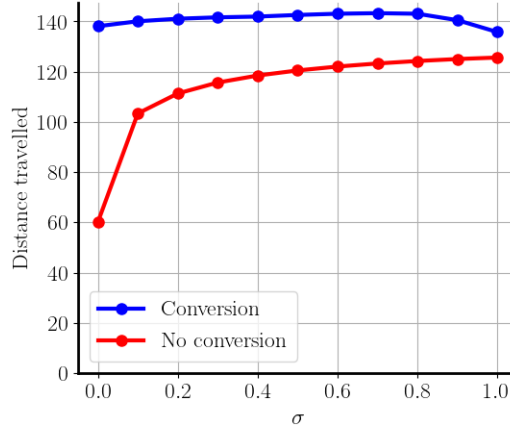
where  $J_u, J_v$  are the inward leader and cell fluxes, respectively. For  $t > 100$ , we applied zero-flux boundary conditions on the cell densities. Finally, the chemoattractant was subject to zero-flux boundary conditions during the entire simulation.

We plotted the distance travelled by the front of the invasion wave<sup>2</sup> at  $t = 300$  for different  $\sigma$  in Figure 4.1a, as well as the total mass of the cells that is present in the domain in Figure 4.1b (data labelled “no conversion” in both figures). For a better estimation of the quality of the invasion, we used a bar chart to represent the mass where the bars were split in proportion to the mass that invaded either the left half or the right half of the domain. We consider the positive  $x$ -direction to go from left to right, so the left and right half correspond to  $[0, L/2]$  and  $[L/2, L]$ , respectively. Finally, we plotted the cell and chemoattractant profiles at  $t = 300$  for the specific case  $\sigma = 0.5$  in Figure 4.2a.

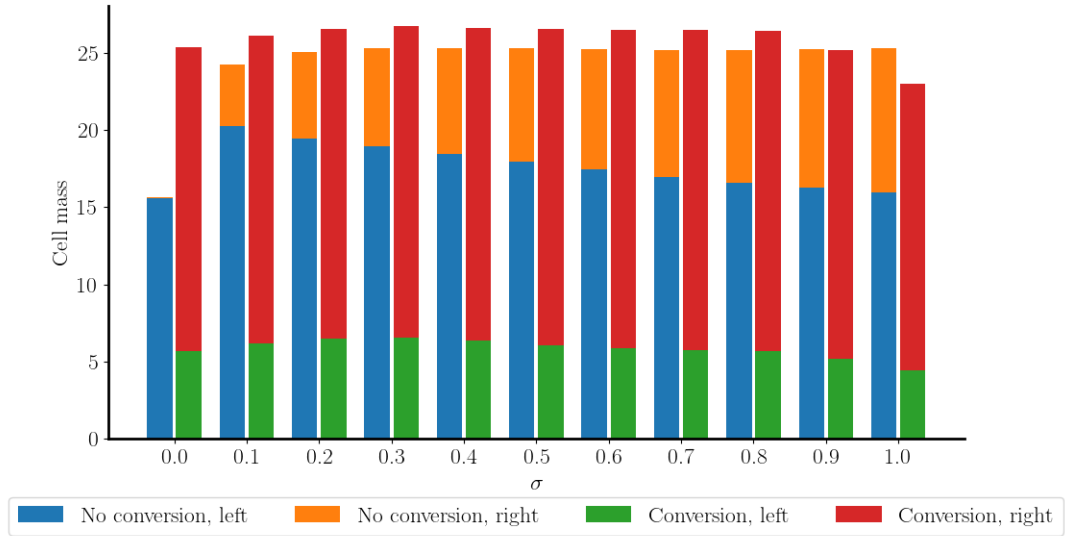
These preliminary results are not particularly encouraging. Figure 4.1a shows that the cells in the leader-only model, corresponding to the case  $\sigma = 1$  where only leader cells are introduced to the system, travel a larger distance than the leader-follower model for any  $\sigma < 1$  that we simulated. Even worse, the results suggest that the

---

<sup>2</sup>The distance travelled at some time  $t$  was defined as the location  $\hat{x}_m$  such that the integral  $\int_0^{\hat{x}_m} (u + v) dx = M - m$ , where  $M = \int_0^L (u + v) dx$ ,  $u$  and  $v$  are evaluated at time  $t$  and  $0 < m \ll M$  is a small constant leading mass. The constant  $m$  is chosen heuristically to provide a reasonable estimation of the leading edge of the wavefront.



(a) Distance travelled by cell population at  $t = 300$  versus  $\sigma$ . The leading mass  $m$  was chosen to be 1.



(b) Bar chart of mass at  $t = 300$  versus  $\sigma$ . Lower part of bar corresponds to mass in the first half of the domain  $[0, L/2]$ , while upper part corresponds to second half  $[L/2, L]$ .

Figure 4.1: Numerical results for simulation of direct leader–follower model without conversion (4.9) and with conversion (4.1), see text for description of numerical simulation. Left column of each pair of bars corresponds to model without conversion and right column to model with conversion. Parameter values are given in Table A.3.

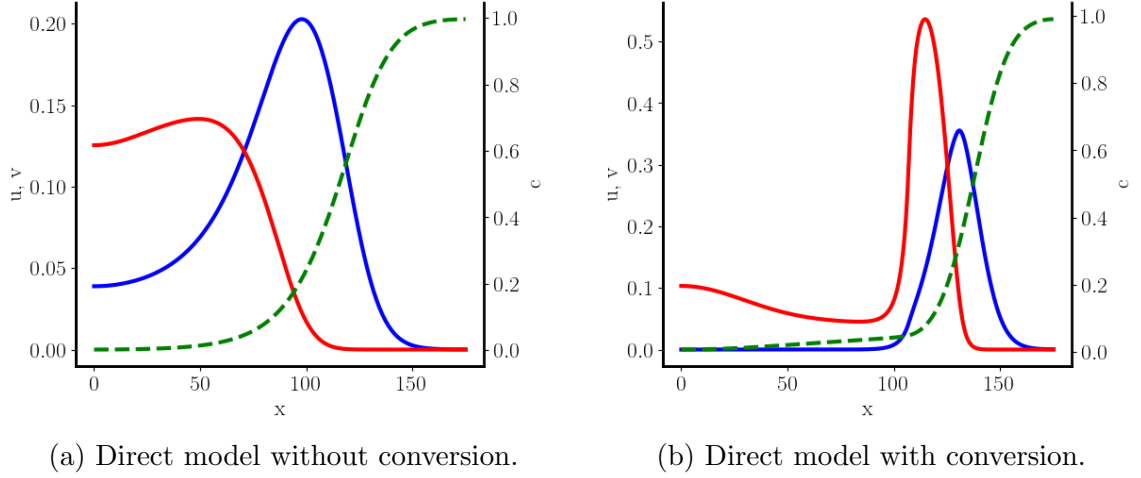


Figure 4.2: Profiles obtained at  $t = 300$  with  $\sigma = 0.5$  for numerical simulation in Figure 4.1. Solid blue and red lines are density profiles of  $u$  and  $v$ , respectively. Green dashed lines are concentration profiles of  $c$ .

distance travelled is a monotonically increasing function of  $\sigma$ . This suggests that the only effect of the addition of followers is to slow down the invasion. A sharp drop in distance travelled occurs for  $\sigma = 0$ , which corresponds to a follower-only model where cell transport happens purely by diffusion.

Figure 4.1b shows that the total number of cells that enter the system, on the other hand, is relatively robust with respect to  $\sigma$ , except for the follower-only case ( $\sigma = 0$ ). However, the proportion of cells that reach the right half of the domain  $[L/2, L]$  decreases when reducing  $\sigma$ . This demonstrates that adding followers results in a degradation of long-distance cell migration on the population level.

The reason for the poor performance of (4.1) is that not much has changed from the point of view of the leaders. The only coupling between the leaders and followers, apart from the non-crowding boundary conditions, is through their joint consumption of the chemoattractant. This does not meaningfully impact the chemoattractant gradient however, as Figure 4.2a shows. Hence, they are essentially behaving as a less populous leader population.

The aim of the leader–follower model is to compensate for the lack of chemoattractant gradient *behind* the wavefront for the leaders to pursue. As opposed to the IBM, the followers in this model do not latch on to the leaders, but are instead guided by a leader gradient. Since the leader dynamics are still largely dominated by diffusive behaviour behind the wavefront, their density profile is relatively smooth. As a



result, the followers are not strongly directed and do not compensate for the lower overall proportion of leaders in the system.

## 4.2 Cell Differentiation

Fortunately, a leader–follower system allows us to hypothesise additional cell interactions that are able to improve upon the leader-only model. Specifically, we assume that the two cell types are capable of converting into each other in a way that maximises the total amount of chemotactic activity. Since leaders become ineffective once they drop behind the chemotactic front, they should differentiate into followers so they can contribute to leader-induced cell fluxes instead. Conversely, a follower cell that has advanced into the leading edge of the wavefront does not experience a strong gradient in the leader cell density, or may even be pulled backwards if it has gone beyond the leader density peak. Such a cell is therefore more useful as a leader.

We assume that these differentiation processes are triggered by the local concentration of chemoattractant for two reasons. First of all, the wavefront is characterised by a sharp rise in  $c$  and thus it forms a natural indicator of a cell’s relative position within the wave. Secondly, the cells are already assumed to be interacting with the chemoattractant in a concentration-dependent way, so they already have access to the necessary information. Letting  $F$  and  $G$  denote the transition rates of leaders to followers and followers to leaders, respectively, and assuming first-order reactions, we define

$$F(u, c) = k_f u (1 - H(c - c_f)) , \quad (4.7)$$

$$G(v, c) = k_g v H(c - c_g) , \quad (4.8)$$

where  $k_f, k_g > 0$  are rate constants, and  $c_f, c_g > 0$  are threshold values, assumed to be constant. When  $c$  drops below  $c_f$ , the leaders recognise that they are lagging behind and thus differentiate into followers. Similarly, followers that find themselves sensing a concentration of  $c$  exceeding  $c_g$  adjust accordingly by adopting a leader phenotype. Based on the chemoattractant concentration, every cell should be either a follower or a leader, so we assume that these conditions do not overlap. This is achieved by imposing  $c_g > c_f$ . The direct leader–follower model with cell differentiation is then

given by

$$\frac{\partial u}{\partial t} = -\nabla \cdot (u\chi_u(c)\nabla c - D_u\nabla u) - F(u, c) + G(v, c), \quad (4.9a)$$

$$\frac{\partial v}{\partial t} = -\nabla \cdot (v\chi_v(u)\nabla u - D_v\nabla v) + F(u, c) - G(v, c), \quad (4.9b)$$

$$\frac{\partial c}{\partial t} = D_c\nabla^2 c - \alpha(u + v)c. \quad (4.9c)$$

Since the differentiation terms couple the leaders and followers more tightly, we expect a larger deviation from the leader-only model. Indeed, Figure 4.2b shows that cell differentiation results in a segmentation of the wavefront. Leaders cells that would previously diffuse away from the leading edge and fail to contribute to further cell invasion are, instead, converted to followers that trail the wavefront indirectly. Simultaneously, the conversion from leaders to followers creates a sharp gradient in the leader density, which provides the followers with a strongly directed signal. This is similar to the principle of cells moving up a cell-induced chemoattractant gradient. The difference here is that the gradient is created by conversion instead of consumption.

We repeated the numerical experiment of Section 4.1 with cell differentiation and found that it resulted in significant improvements with respect to cell migration. First of all, the distance travelled is larger for the  $\sigma$  that we simulated (Figure 4.1a). Moreover, the variability of the travelled distance with respect to  $\sigma$  was greatly reduced, indicating that the system is robust with respect to type of cells that enter the domain. Secondly, Figure 4.1b demonstrates that the total amount of cells entering the domain is somewhat higher than without differentiation, except for  $\sigma$  close to one. The important difference, however, lies in the number of cells that reach the second half of the domain. For every simulation, at least three quarters of the cells reach the right part of the domain. In addition, the proportion of cells that migrate further is much more consistent across different values of  $\sigma$  than the non-differentiating model.

### 4.2.1 Leader-Induced Cell-Crowding

An interesting contrast with the non-differentiating model is that the cell mass injected and the distance travelled both experience a dip for  $\sigma = 1$ , i.e. when only leaders cells enter the domain for  $t \in (0, 100]$ , whereas this is the optimal case for the non-differentiating model. This points to a non-trivial difference in behaviour, so we plotted the cell densities of the differentiating model at  $t = 100$  for a leader-only

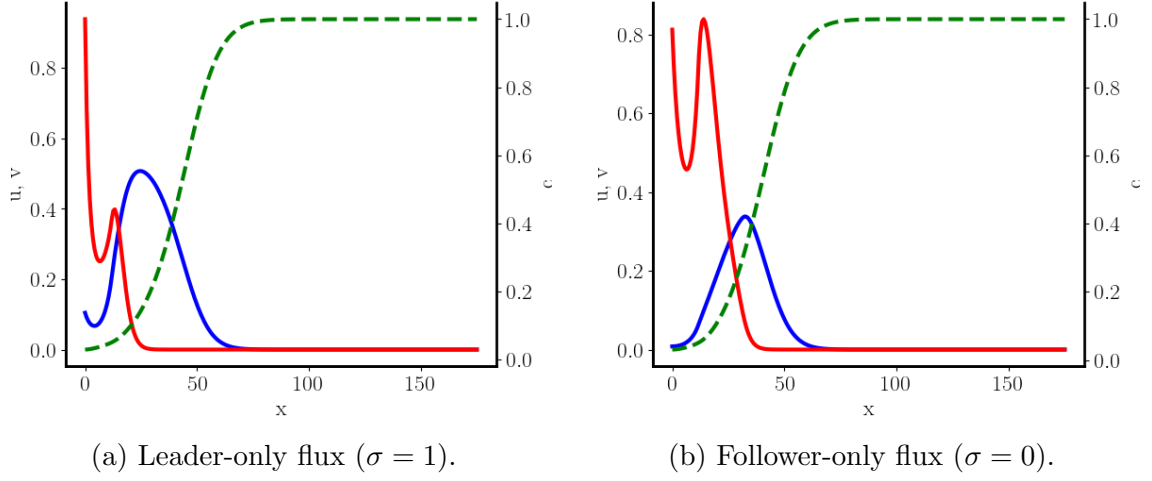


Figure 4.3: Cell profiles obtained at  $t = 100$  for leader-only flux ( $\sigma = 1$ ) and follower-only flux ( $\sigma = 0$ ) for numerical simulation in Figure 4.1. Solid blue and red lines are density profiles of  $u$  and  $v$ , respectively. Green dashed lines are concentration profiles of  $c$ .

flux (Figure 4.3a) and a follower-only flux (Figure 4.3b), corresponding to  $\sigma = 1$  and  $\sigma = 0$ , respectively.

Both figures display a formation of leaders and followers. In the case of a follower-only flux this is guaranteed to be the case for  $t > 0$  since the initial chemoattractant concentration is above the threshold value  $c_g$ . For the leader-only flux simulation, only leaders are present initially. The conversion of followers is initiated when sufficient chemoattractant has been consumed so that it reaches values below  $c_f$ . We see that the combined inward flux and differentiation of leader cells at the boundary causes a locally convex profile in  $u$ . This induces a cytotoxic flux of followers towards the boundary, causing followers to crowd at the boundary. The zero-flux boundary condition on  $v$  dictates that the cytotoxic flux is counteracted by a diffusive flux, resulting in a sharp spike in the follower profile and thus a high total cell density at the boundary. Because of the non-crowding cell flux (4.4), new leader cells are then blocked from entering the domain. This explains why the differentiating cell model performed worse than expected for  $\sigma = 1$ .

### 4.2.2 Self-Organisation

In order to investigate the conversion dynamics separately from any boundary phenomena, we repeated the experiment without cells entering the domain (zero-flux boundary conditions). Instead, we filled a subinterval  $[0, d]$ , where  $d < 175$  is a non-negative constant, with a fixed total amount of cells at the start of the simulation  $t = 0$ , but with varying proportions of leaders and followers, as determined by  $\sigma$ . The initial conditions for  $u$  and  $v$  were thus

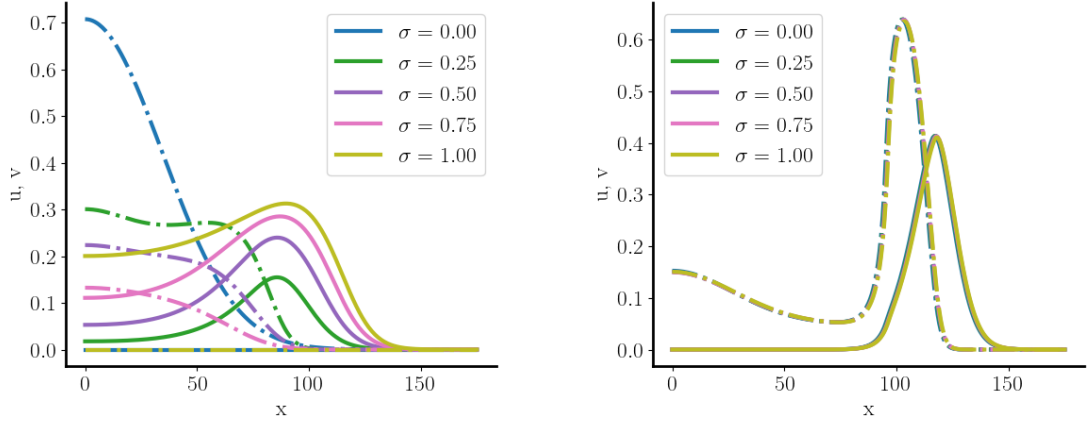
$$u(x) = \sigma (1 - H(x - d)) \quad \text{at } t = 0, \quad (4.10)$$

$$v(x) = (1 - \sigma) (1 - H(x - d)) \quad \text{at } t = 0. \quad (4.11)$$

Other than the initial and boundary conditions for  $u$  and  $v$ , the remaining conditions and parameters were left unchanged.

We plotted the cell profiles at  $t = 200$  for different  $\sigma$  in Figures 4.4a and 4.4b for the direct model without conversion and with conversion, respectively, and with  $d = 30$ . The figures demonstrate that the introduction of cell differentiation results in the cells evolving to a distribution that is insensitive to the initial conditions. This shows that a differentiation scheme based on relatively simple rules, such as the one defined by (4.7) and (4.8), is sufficient to generate a self-organising wavefront with a robust structure.

We have established in Section 4.2.1 that a leader-only flux results in cell-crowding once the chemoattractant reaches concentrations below  $c_g$ . On the other hand, we have demonstrated here that the wavefront structure generated by cell differentiation is robust with respect to the initial proportions in the cell population. Together, these observations suggest that a simple and reliable method to populate the neural crest is to inject only follower cells. This avoids cell-crowding at the entrance and has little impact on the robust leader–follower dynamics taking place further away from the boundary. Although it cannot be ruled out that the neural tube is sensitive to the chemoattractant and introduce different cell types based on the local chemoattractant concentration or other factors, we note that the self-organising properties of the current model render such mechanisms redundant. For simplicity, we will assume a follower-only flux hereafter.



(a) Cell profiles at  $t = 200$  without conversion for different  $\sigma$ . (b) Cell profiles at  $t = 200$  with conversion for different  $\sigma$ .

Figure 4.4: Cell profiles obtained at  $t = 200$  for the numerical solution of the direct model without boundary cell fluxes, see text for details on description of numerical simulation. Parameters were the same as in Figure 4.1. The solid and dash-dotted lines are the profiles of  $u$  and  $v$ , respectively.

### 4.3 Cell Flux Analysis

As a test case for NC cell migration, we simulated the differentiating leader–follower model on the one-dimensional domain  $[0, L]$  with a non-crowding, follower-only flux boundary condition at  $x = 0$  and the initial conditions (4.2). For comparison, we simulated the leader-only model on the same domain with a non-crowding, leader-only flux boundary condition at  $x = 0$  and the same initial conditions for the leaders and the chemoattractant. All remaining boundary conditions in both simulations were zero-flux.

Our hypothesis is that the leader–follower model increases the number of cells participating in chemotaxis, so we characterised the cell migration activity using a visualisation method adapted from [23]. At regular time intervals, we computed the “cutpoints” that distribute the total cell mass evenly into  $q$  contiguous intervals that cover the domain (this is the same concept as quantiles for statistical distributions). Formally, we define the points  $x_i \in [0, L]$ ,  $i = 0, 1, \dots, q$  that have the property

$$\int_{x_i}^{x_{i+1}} (u + v) dx = \frac{1}{q} \int_0^L (u + v) dx \quad \text{for } i = 0, 1, \dots, q - 1, \quad (4.12)$$

and  $x_i < x_j$  if  $i < j$ , with  $x_0 = 0$ ,  $x_q = L$ . We integrated the leader and cell fluxes in

each interval  $[x_i, x_{i+1}]$ <sup>3</sup>,

$$(P_u)_i = \int_{x_i}^{x_{i+1}} J_u(u, c) dx = \int_{x_i}^{x_{i+1}} \left[ u \chi_u(c) \frac{\partial c}{\partial x} - D_u \frac{\partial u}{\partial x} \right] dx, \quad (4.13)$$

$$(P_v)_i = \int_{x_i}^{x_{i+1}} J_v(u, v) dx = \int_{x_i}^{x_{i+1}} \left[ v \chi_v(u) \frac{\partial u}{\partial x} - D_v \frac{\partial v}{\partial x} \right] dx, \quad (4.14)$$

and write  $(P_{u+v})_i = (P_u)_i + (P_v)_i$ . Using analogous definitions for the leader-only model, we plotted the results side by side in Figure 4.5a using a heat map.

For the leader-only model, a distinctive separation develops between the chemotactic front and the cells that are dominated by diffusion. The boundary between chemotactic cells and diffusive cells coincides roughly with the point where  $c = \beta$ . This is in agreement with our discussion of non-singular chemotaxis in Section 3.3, where we concluded that the failure of non-singular chemotaxis occurs when  $c$  reaches levels on the order of  $\beta$ . Because the point  $c = \beta$  indicates the transition from chemotactically dominated to diffusion dominated cell motion, we call it the **chemotactic boundary**.

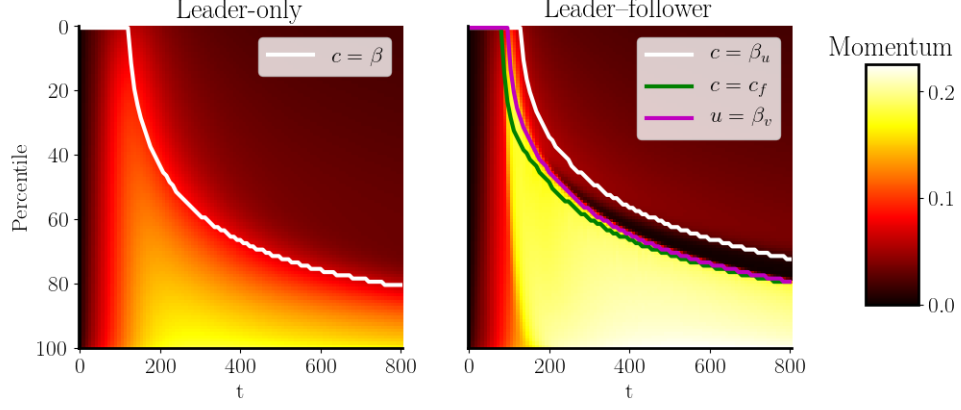
On the other hand, the heat map for the leader-follower model shows that a higher portion of the cell population is actively migrating and at an increased rate. Moreover, since the trailing part of the chemotactic front is populated by followers instead of leaders, the chemotactic boundary is not given by  $c = \beta_u$ , but  $u = \beta_v$  instead. We also plotted the leader and follower fluxes separately in Figure 4.5b. The figure demonstrates that the leaders and followers contribute to distinct segments of the wavefront.

Although we have demonstrated a higher level of chemotactic activity, the cell flux analysis also points to a limitation of the direct leader-follower model. In the mathematically ideal case of a sufficiently singular chemotactic sensitivity, as described in Chapter 3, the cell flux behind the wavefront is approximately constant. In contrast, the direct leader-follower dynamics results in an abrupt drop in the cell flux behind the wavefront, as Figure 4.5a shows. This results in a sparsely populated region between the neural crest and the wavefront, as shown in Figure 4.6a.

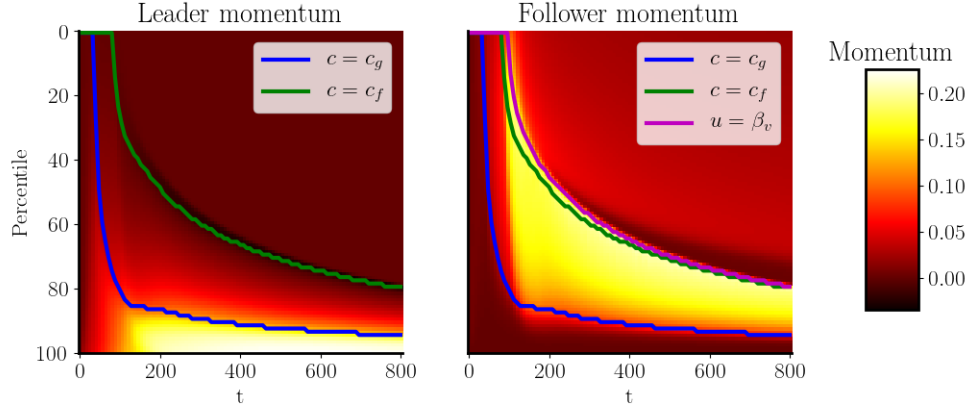
The reason for this is that the chemotactic boundary of the followers, given by  $u = \beta_v$ , closely trails the point where leaders start converting to followers, given by  $c = c_f$ . As the leaders differentiate to followers, their cell density drops quickly, which

---

<sup>3</sup>Physically speaking, integrating a mass flux over a part of the domain yields the total momentum contained in that subdomain, hence we use the symbol  $P$ . However, we will use the terms momentum and flux interchangeably to refer to the amount of cell migration.

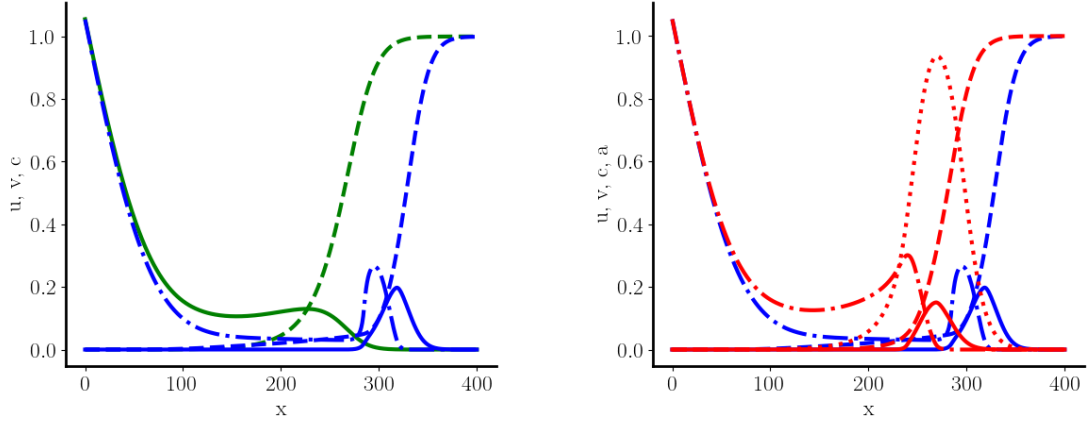


(a) Comparison of leader-only model with direct leader-follower model.



(b) Decomposition of cell momentum into leader and follower momentum in direct leader-follower model.

Figure 4.5: Heat maps of cell momentum in test case simulation of leader-only model and direct leader-follower model on the domain  $[0, 400]$  for  $t \in (0, 800]$ . See text for details on the visualisation method, boundary conditions and initial conditions. Solid lines indicate where functions reached particular values as indicated in the legend. If the function reached the value for multiple positions in the domain, only the relevant position was plotted. In the case of  $u = \beta_v$ , this was the one closest to  $x = 0$ . Parameters for leader-follower model were reused from Figure 4.1. Identical parameters were used for leader-only model where applicable. We used  $q = 100$  intervals and plotted the results at intervals of 8 time units.



(a) Profiles for leader-only (green) and direct leader-follower model (blue). (b) Profiles for direct (blue) and indirect leader-follower model (red).

Figure 4.6: Profiles of leader and follower densities and chemoattractant concentration at  $t = 800$  for the simulations in Figure 4.5 and Figure 4.7. Solid, dash-dotted, dashed and dotted lines represent  $u$ ,  $v$ ,  $c$  and  $a$ , respectively.

narrowly confines the region of active follower chemotaxis. The consequence is that the followers form a mobile, but compact wavefront structure with the leaders. This is in contrast to observations of NC cell migration, which show that the cells migrate in a coherent stream [1, 2].

### 4.3.1 Indirect Model

We can decouple follower chemotaxis from cell differentiation by assuming that the leaders and followers interact indirectly through a chemical. In a similar way that leaders pursue a gradient in  $c$ , the followers are assumed to be guided by a gradient in a chemical produced by the leaders. We have demonstrated the importance of a cell-induced gradient for directed chemotaxis in Chapter 3, and thus assume that the followers consume this additional chemical to generate a favourable chemotactic gradient.

Denoting the additional chemical at position  $\mathbf{x}$  and time  $t$  by  $a(\mathbf{x}, t)$ , and assuming its production is proportional to the leader cell density  $u$ , the indirect model is



described by

$$\frac{\partial u}{\partial t} = -\nabla \cdot (u\chi_u(c)\nabla c - D_u\nabla u) - F(u, c) + G(v, c), \quad (4.15a)$$

$$\frac{\partial v}{\partial t} = -\nabla \cdot (v\chi_v(a)\nabla a - D_v\nabla v) + F(u, c) - G(v, c), \quad (4.15b)$$

$$\frac{\partial c}{\partial t} = D_c\nabla^2 c - \alpha_c(u + v)c, \quad (4.15c)$$

$$\frac{\partial a}{\partial t} = D_a\nabla^2 a - \alpha_a va + r_a u(a_{\max} - a), \quad (4.15d)$$

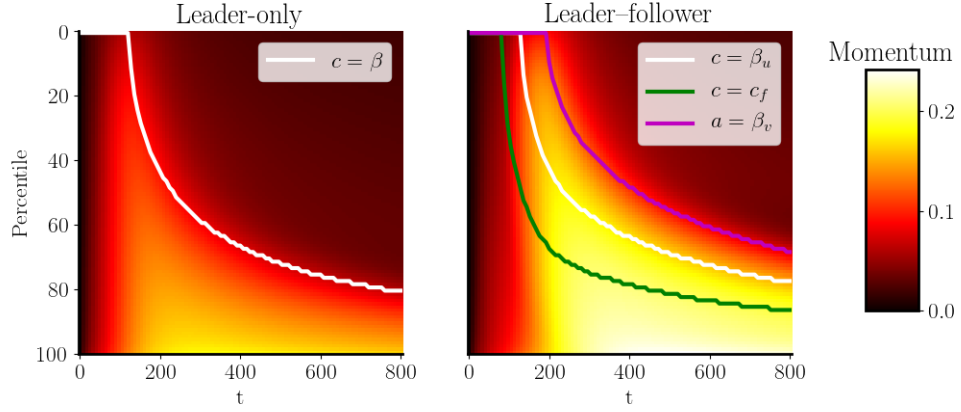
where  $\chi_v(a)$  is the chemotactic sensitivity of  $v$  as a function of  $a$ , assumed logarithmic with chemotactic coefficient  $k_v$  and saturation constant  $\beta_v$ ,  $r_a > 0$  is the production constant of  $a$ ,  $D_a > 0$  is the constant diffusion coefficient of  $a$ , and  $\alpha_c, \alpha_a > 0$  are the consumption constants of  $c$  and  $a$ , respectively. In order to avoid the concentration of  $a$  growing beyond realistic bounds, we assume that the system has a finite carrying capacity for  $a$ , given by the non-negative constant  $a_{\max}$ .

Repeating the test case simulation for the indirect model and plotting the cell flux (see Figure 4.7) shows that it is successful in separating the chemotactic boundary of the followers, given by  $a = \beta_v$ , from the initiation of leader to follower cell differentiation, given by  $c = c_f$ . This results in a smoother transition from chemotactic to diffusive behaviour in follower cells. Although Figure 4.6b shows that the indirect model does not travel as far as the direct model, the figure also shows that the invasion stream is much more coherent.

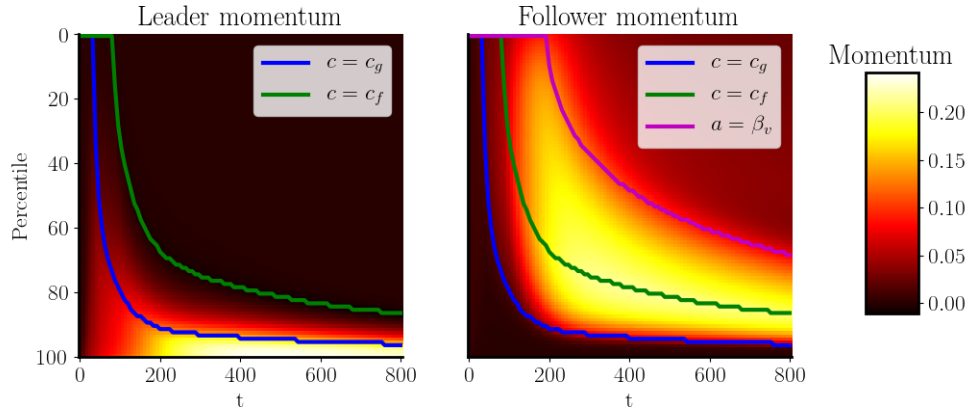
The robustness and self-organising properties of the direct leader–follower model carry over to the indirect leader–follower model, but we will leave out a thorough analysis of the indirect model here and instead discuss a generalised model in Chapter 5.

## 4.4 Discussion

In this chapter, we first proposed a leader–follower model based on short-range, direct interactions between leader and follower cell types. Numerical experiments then demonstrated that the direct model fails to improve cell migration for fixed cell subpopulations (Section 4.1), but performs much better when the cells are able to differentiate (Section 4.2). However, a pathological case occurs when the neural crest only releases leader cells. The combination of an inward leader cell flux and the conversion to follower dynamics results in cell-crowding, preventing new cells from entering



(a) Comparison of leader-only model with indirect leader-follower model.



(b) Decomposition of cell momentum into leader and follower momentum in indirect leader-follower model.

Figure 4.7: Heat maps of cell momentum in test case simulation of leader-only model and indirect leader-follower model, obtained in the same way as in Figure 4.5. Parameter values are given in Table A.4.

the domain. Since we also showed that the leader–follower dynamics are robust with regards to the initial proportion of leaders and cells, we proposed a follower-only flux to avoid cell-crowding.

In Section 4.3, we simulated a test case for the direct, differentiating leader–follower model with a follower-only flux and found that it achieves long-distance cell migration and increases the number of cells actively migrating. However, it also gave rise to an incoherent cell stream, which contradicts experimental results. This issue was alleviated by assuming an indirect interaction between leaders and followers that decouples the chemotactic activity of followers from the leader to follower cell differentiation.

For both the direct and indirect leader–follower models, the volume of cell migration was increased by a division of the cell population into subpopulations that respond to different stimuli. The leader population assumed the same role as the cells in the leader-only model in Chapter 3, moving up a cell-induced gradient of the chemoattractant  $c$ . The followers then trailed the leader population by responding directly or indirectly to the leader cells, pushing the chemotactic boundary of the whole cell population back and increasing the total cell flux. The robustness of leader–follower dynamics rests fundamentally on cell differentiation processes that ensure that the wavefront self-organises into a stereotypical leader–follower structure. We also note that transplantation experiments in chick embryos have demonstrated that cranial NC cells are capable of differentiating into leader or follower phenotypes [1, 2].

Although we have constructed a “fix” to increase the range of chemotaxis in comparison with the leader-only model, it is only a temporary fix. For a large enough time, a sufficient number of cells will be lost at the chemotactic boundary of the leader–follower population such that a majority of the cells are undirected, similarly to how the wavefront loses cells to diffusion in the leader-only model. In the next chapter, we will address this issue by showing that the leader–follower dynamic described here is a scalable mechanism.

# Chapter 5

## Chain Model

In the previous chapter, we saw that the key principle in the leader–follower model is the differentiation of cells into subtypes based on their relative position in the wavefront. With relatively simple differentiation rules, we were able to construct a model where cells self-organise into a segmented wavefront that increases the overall chemotactic activity of the cell population. The chemotactic boundary was pushed back by having the follower population respond to a secondary signal, created directly or indirectly by the leader cells. However, the leader–follower model merely delays the inevitable because the chemotactic boundary has not been eliminated. The model is only able to “catch” the leaders that would normally drop out and convert them to followers, but offers no such mechanism for the followers.

The indirect leader–follower model offers an interesting parallel between the leaders and the followers. They essentially have the same chemotactic behaviour, but for different chemoattractants. The similarity in behaviour also helps explain the failure of the leader–follower model, because the followers suffer from the same issue as the leaders in the leader-only model. Recognising this, we can iterate and introduce a third cell type that trails the follower cell type in the same way that followers trail the leaders. Likewise, this does not eliminate the chemotactic boundary but the key point is that we can iterate until we have sufficient cell types to produce a coherent cell stream that fills the cranial NC crest pathway. This is the basis of the **chain model**.

## 5.1 Generalisation of Indirect Model

To formulate this model for a system with  $N$  cell types, we label the cell populations as  $u_n$ , where  $n = 1, 2, 3, \dots, N$  is the cell type index counting from the wavefront towards the neural tube. Thus,  $u_1$  corresponds to the cell type at the leading edge of the wavefront. The chemoattractant to which  $u_n$  is given the same index  $n$ , hence  $c_n$  attracts cell type  $u_n$ . Under this convention,  $c_1$  is the only chemoattractant that is *not* produced by any cells. The indirect model in Section 4.3.1 corresponds to the case  $N = 2$  with the mapping  $(u, v, c, a) \leftrightarrow (u_1, u_2, c_1, c_2)$ .

When describing the relative position of cell populations  $u_n$  and  $u_m$  where  $n > m$ , we say that  $u_n$  trails  $u_m$  and  $u_m$  leads  $u_n$ . Likewise, we say that the chemoattractant  $c_m$  leads  $u_n$  if  $m \leq n$  and that  $c_m$  trails  $u_n$  for  $m > n$ . This ordering is visualised as follows:

$$\left. \begin{array}{l} u_N, \dots, u_{n+1} \\ c_N, \dots, c_{n+1} \end{array} \right\} \xrightarrow{\text{trails}} u_n \xleftarrow{\text{leads}} \left\{ \begin{array}{l} u_{n-1}, \dots, u_1 \\ c_n, \dots, c_1 \end{array} \right.$$

Zooming in on the direct interactions of a cell type with its neighbouring cell types and chemoattractants, we say that the trailing population  $u_{n+1}$  follows  $u_n$ , while  $u_n$  guides  $u_{n+1}$ . For chemoattractants, we say that  $c_n$  attracts  $u_n$  and  $c_{n+1}$  is produced by  $u_n$ . These direct interactions are summed up by the following diagram:

$$\begin{array}{ccccc} u_{n+1} & \xrightarrow{\text{follows}} & u_n & \xleftarrow{\text{guides}} & u_{n-1} \\ & & & & \\ c_{n+1} & \xleftarrow{\text{produces}} & & \xleftarrow{\text{attracts}} & c_n \end{array}$$

In both these diagrams, the neural tube is placed on the left of the page, with the cell migration directed towards the right.

It is important to carefully consider the conditions for cell differentiation. In the leader–follower model, the follower cells convert to leaders when they perceive a high concentration of the chemoattractant that attracts the leaders. Translated to the chain model with  $N = 2$ , this means that when the cells  $u_2$  sense an abundance of the chemoattractant  $c_1$ , which attracts its guiding cells  $u_1$ , they will convert to  $u_1$ . For the case  $N = 3$ , it seems logical then to suggest that  $u_3$  converts to its guiding population  $u_2$  at high concentrations of  $c_2$ . However, consider a system where initially only  $c_1$  is present and we inject the cell type  $u_3$ . If the conversion to  $u_2$  can only be triggered by  $c_2$ , then no cell differentiation to  $u_2$  will ever take place since  $c_2 = 0$ . This creates a gap in the cell differentiation chain since only  $u_2$  can convert to  $u_1$ . Thus, no cells differentiate into the type  $u_1$  that moves up gradients of  $c_1$ , and cell migration is never initiated.

This is resolved by having cells convert to their guiding cell type when they perceive high amounts of the chemoattractants that attract not only their guiding cell type, but *all* leading cell types. We implemented this by summing over the concentrations of all leading chemoattractants, hence

$$G_n(u_n, c_1, c_2, \dots, c_{n-1}) = k_g u_n H \left( \sum_{j=1}^{n-1} c_j - c_g \right), \quad (5.1)$$

where  $k_g, c_g$  have the same meaning as in Section 4.2. Defining the follower cell to guiding cell transition rate in this way ensures that cells always convert to successive leading cell types until they reach the type that responds to the most leading chemoattractant present. In our example, this means that  $u_3$  converts to  $u_2$  and then to  $u_1$  in the presence of  $c_1$ .

Similarly, we let the conversion of cells to trailing cell types be determined by a lack of its attracting chemoattractant and all leading chemoattractants. This avoids cells prematurely converting to trailing types when there are still chemoattractants present that attract their leading types:

$$F_n(u_n, c_1, c_2, \dots, c_n) = k_f u_n \left[ 1 - H \left( \sum_{j=1}^{n-1} c_j - c_f \right) \right] \quad (5.2)$$

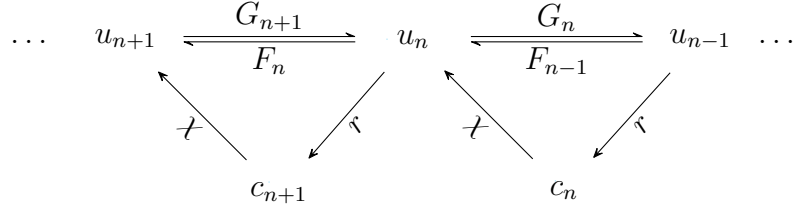
where  $k_f, c_f$  have the same meaning as in Section 4.2.

We assume that all cell types and chemoattractants have similar properties. For the cells, this means that they obey the same chemotactic law  $\chi(\cdot)$  and have the same constant diffusion coefficient  $D_u > 0$ . Similarly, all chemoattractants are assumed to be consumed with the consumption constant  $\alpha > 0$ , produced with the production constant  $r > 0$  and have the constant diffusion coefficient  $D_c > 0$ . The  $N$ -chain leader–follower model is thus defined by

$$\begin{aligned} \frac{\partial u_n}{\partial t} = & -\nabla \cdot (u_n \chi(c_n) \nabla c_n - D_u \nabla u_n) - F_n(u_n, \bar{c}_n) - G_n(u_n, \bar{c}_{n-1}) \\ & + F_{n-1}(u_{n-1}, \bar{c}_{n-1}) + G_{n+1}(u_{n+1}, \bar{c}_n), \end{aligned} \quad (5.3a)$$

$$\frac{\partial c_n}{\partial t} = D_c \nabla^2 c_n - \alpha c_n \sum_{j=n}^N u_j + r u_{n-1} (1 - c_n), \quad (5.3b)$$

for  $n = 1, 2, \dots, N$  and where  $\bar{c}_n$  is shorthand for  $c_1, c_2, \dots, c_n$ . The extremal cases  $n = 1, N$  are handled by defining  $F_0 = F_N = G_1 = G_{N+1} = u_0 = 0$ . For  $u_n$ , we schematically depict the cell differentiation, chemotaxis and production processes in relation with its neighbours in the wavefront as follows:



The arrows labelled  $\chi$  and  $r$  represent chemotaxis and production, respectively, where the direction of the arrow in  $X \rightarrow Y$  means “ $X$  appears in the equation of  $Y$ ”. The arrows labelled  $F$  and  $G$  represent conversion rates, with the direction of the arrow in  $X \rightarrow Y$  meaning “ $X$  converts to  $Y$ ”.

## 5.2 Cell Flux Analysis

We now generalise the test case simulation on the one-dimensional domain  $[0, L]$  of the previous chapter to analyse the cell activity in the chain model. As discussed in Section 4.2.1, in the leader–follower model, a leader-only boundary flux at  $x = 0$  results in cell crowding because of followers moving towards the boundary. Similarly, in the chain model, imposing a cell flux for any type other than the most trailing cell type causes cells to cluster at the neural tube and reduces the number of cells entering the system. We therefore apply a non-crowding cell flux at  $x = 0$  on the most trailing cell type  $u_N$ , defined for the chain model as

$$J_{\text{in}}(\overline{u_N}) = g(1 - H_b(u_{\text{total}} - u_{\text{max}})) , \quad (5.4)$$

where  $\overline{u_N}$  signifies  $u_1, u_2, \dots, u_N$ , and  $u_{\text{total}} = \sum_{j=1}^N u_j$  is the total cell density. This is the generalisation of (4.4) and hence the constants and functions that appear in it have the same meaning. We impose zero-flux boundary conditions on all the remaining cell types and on all chemoattractants.

For the initial conditions, we fill the domain with a uniform concentration of  $c_1$ . This is the only chemoattractant not produced by the cells and can be considered as an external signal that guides the cell population as a whole, since all other chemoattractants are produced by the cells. The domain is assumed to be initially devoid of any cells and any chemoattractant produced by the cells.

We generated heat maps indicating the migration activity of cells by generalising the cell flux analysis method described in Section 4.3. In the generalised case, the  $q + 1$  points  $x_i \in [0, L]$  divide total cell mass evenly into  $q$  intervals so that

$$\int_{x_i}^{x_{i+1}} u_{\text{total}} dx = \frac{u_{\text{total}}}{q} \quad \text{for } i = 0, 1, \dots, q - 1 . \quad (5.5)$$

The momentum of  $u_n$  in each interval is then calculated as

$$(P_{u_n})_i = \int_{x_i}^{x_{i+1}} J_u(u_n, c_n) dx = \int_{x_i}^{x_{i+1}} \left[ u_n \chi_u(c_n) \frac{\partial c_n}{\partial x} - D_u \frac{\partial u_n}{\partial x} \right] dx, \quad (5.6)$$

with the total cell flux obtained by summing over all cell populations, i.e.  $(P_{\text{total}})_i = \sum_{j=1}^N (P_{u_j})_i$ .

The test case was simulated for  $N = 1, \dots, 9$ , and the results are given in Figure 5.1. The simulations clearly show that the proportion of cells actively migrating expands significantly as the number of simulated cell types is increased. We also plotted the location where the chemoattractant attracting the most trailing cell type reaches  $\beta$ . In Section 4.3, we reasoned that the chemotactic boundary of the cell population as a whole is given by the chemotactic boundary of the follower cell type, since the leader cells that stay behind convert to followers instead of losing their directionality. In the chain model, a cell goes through many more stages before it reaches the rear of the wavefront. In each of these stages, the cells maintain directed migration by interactions with their guiding cell type. This front-to-back signalling cascade ends at the most trailing cell type  $u_N$ , and thus the chemotactic boundary of the cell population is determined by the trailing cell type.

The figures suggest that adding more cell types introduces a lag period in the cell migration where the cells seem to be less active before the migration stream is fully developed, for instance between  $t = 0$  and  $t = 750$  for  $N = 7$ . However, the quantity displayed in the heat maps is the momentum, the product of mass and velocity, and the total cell mass in the system increases rapidly in the early stages of the simulation. For a better representation of the activity of individual cells, we scaled the momentum at every time  $t$  by the mass contained in that interval to obtain the average velocity:

$$(V_{u_n})_i = \frac{q}{n_{\text{total}}} (P_{u_n})_i, \quad (5.7)$$

and defined the total average velocity as  $(V_{\text{total}})_i = \sum_{j=1}^N (P_{u_j})_i$ . We plotted the results for  $N = 9$  in Figure 5.2, where we left out the first 10 time points to avoid issues when the total cell mass is zero or close to zero. Plotting the heat map of the average cell velocity shows that cell speeds are actually relatively uniform in the left part for  $t < 750$ . The reason for a perceived lag period in Figure 5.1 can thus be attributed to a lower amount of cell mass early on in the simulation.

Figure 5.2 also reveals a banded structure in two places: vertical bands in the upper left-hand corner and horizontal slanted bands in the lower right-hand quadrant. We decomposed the cell momentum into the individual cell types in Figure 5.3 to show that these bands correspond to distinct cell types.



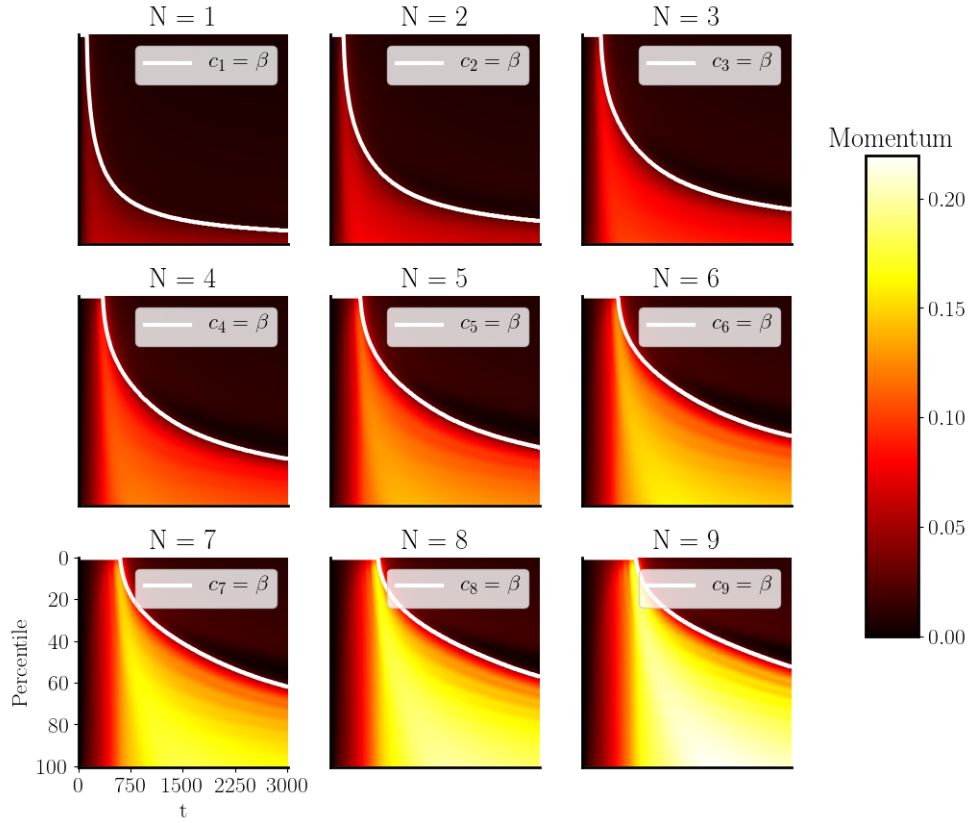


Figure 5.1: Heat maps of cell momentum in test case simulation of chain model for  $N = 1, \dots, 9$ . See text for details on the visualisation method, boundary conditions and initial conditions. Solid lines indicate the chemotactic boundary of the most trailing population. Parameter values are given in Table A.5. We used  $q = 300$  intervals and plotted the results at intervals of 10 time units.

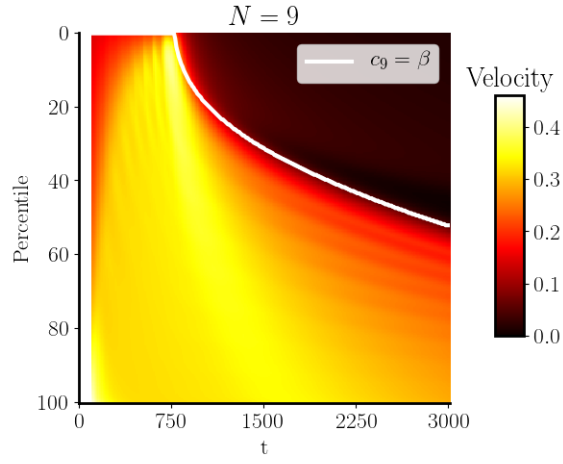


Figure 5.2: Heat map of the cell velocity for simulation in Figure 5.1 with  $N = 9$ .

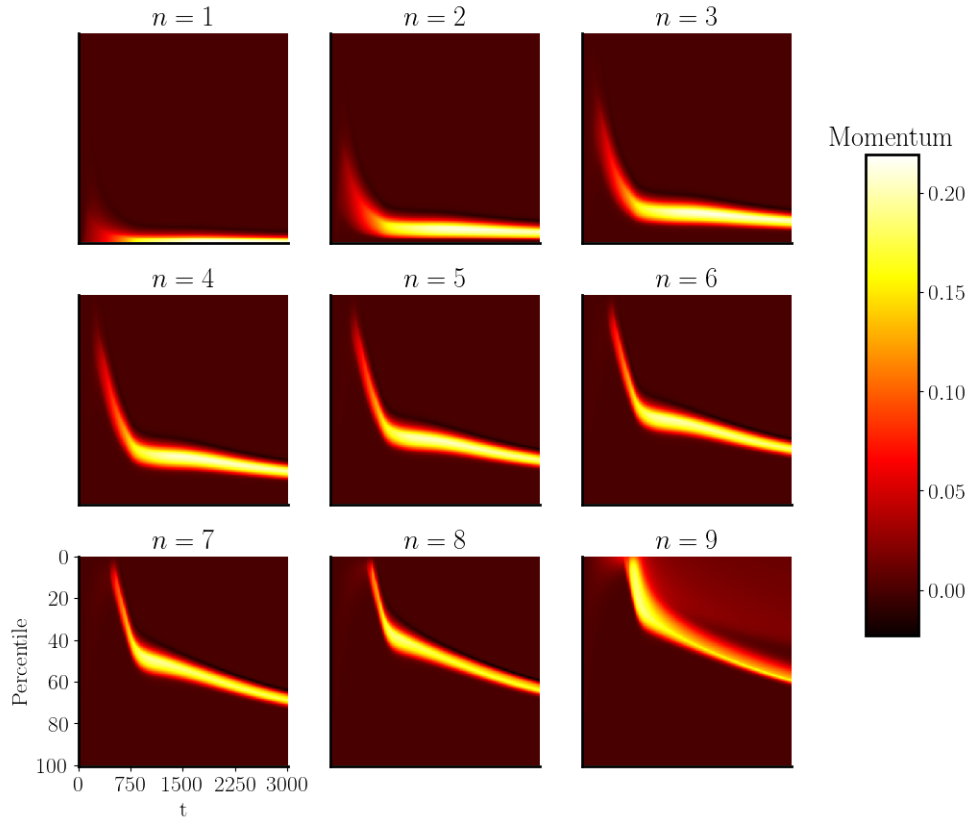


Figure 5.3: Decomposition of the cell momentum into individual cell types for simulation in Figure 5.1 with  $N = 9$ .

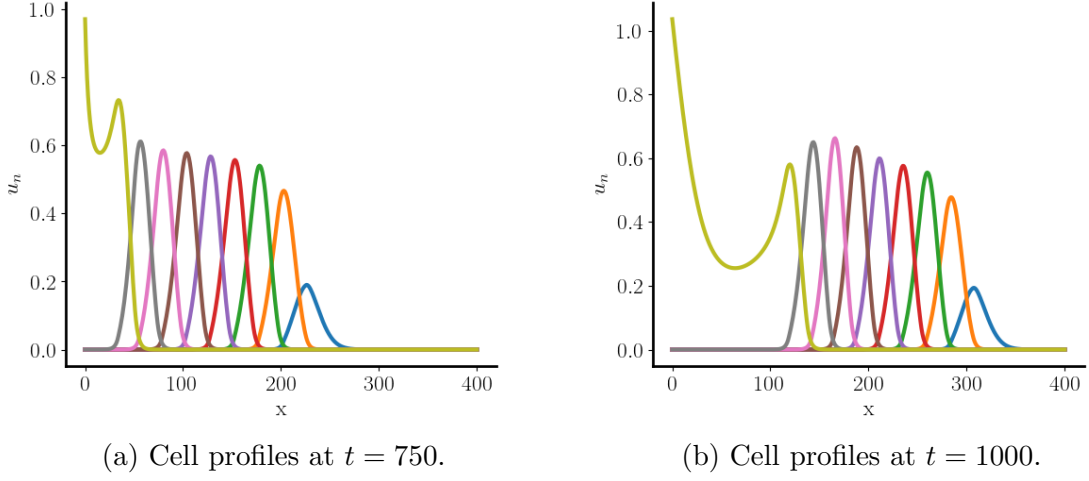


Figure 5.4: Cell profiles obtained at  $t = 750$  and  $T = 1000$  for the numerical simulation in Figure 5.1 with  $N = 9$ . We distinguished the cell types by assigning them different colours. The ordering of the cell types is as described in the text, with the rightmost cell type corresponding to  $u_1$  and the leftmost cell type to  $u_N$ .

### 5.3 Discussion

The decomposition of cell fluxes in Figure 5.3 show that the simulation of the chain model is characterised by two different stages. For  $t < 750$ , the peak of the cell type's individual contribution moves forward rapidly in the cell distribution, and then continues at a much slower pace for  $t > 750$ , resulting in a distinctive kink in the heat map. The transition coincides roughly with the chemotactic boundary of  $u_N$  moving away from the neural tube, suggesting that it coincides by the trailing population  $u_N$  starting to migrate with the wavefront. Plotting the cell profiles for  $t = 750$  and  $t = 1000$  (Figure 5.4) shows that this is indeed the case.

To understand why the system behaviour changes so drastically, consider first the early stages of the simulation. The trailing cell type  $u_N$  is the first cell type to enter the system, but these cells immediately convert to its guiding cell type in the presence of  $c_1$  (see definition of  $G_n$  in Section 5.1). All subsequent cell types, except for  $u_1$ , also convert to their guiding cell types. As a result, the cell flux of  $u_N$  effectively feeds into the cell population  $u_1$ . Regardless of type, all cells consume  $c_1$  and thus a gradient in  $c_1$  will develop very quickly. This causes the cells of type  $u_1$  to break away from the boundary as they pursue a cell-induced gradient in  $c_1$ .

During this event, the composition of chemoattractants at the boundary changes

in two important ways. First of all, the departure of  $u_1$  implies that the concentration at the boundary has dropped to significantly lower levels, else there would not be a sufficiently steep gradient for  $u_1$  to pursue. As a result, the cells of type  $u_2$  stop converting to their guiding type and become more numerous. Secondly, as  $u_1$  moves away from the neural tube, so does the only source of the chemoattractant  $c_2$ . This leaves the cells  $u_2$  in the same situation that the leading population  $u_1$  was in at the start: they are not being converted to leading cell types, and they become directed away from the boundary as a result of a cell-induced gradient in their chemoattractant. We thus conclude that the departure of  $u_1$  from the neural tube simultaneously creates the conditions for the departure of  $u_2$ . The departure of  $u_2$  in turn triggers the departure of  $u_3$ , resulting in a cascade where successive cell types emerge from the boundary. Meanwhile, the cell flux of  $u_N$  is continuously feeding into the departing cell populations.

Eventually however, the trailing cell type  $u_N$  will start migrating with the wave-front. Any new cells entering the domain are no longer converted into successive leading types, but are instead limited by the migration of  $u_N$ , which is driven by a cell-induced gradient in  $c_N$ . As we saw in previous chapters, a chemotactic boundary will appear over time, and thus the rate at which new cells are added to the system becomes limited by the diffusion of  $u_N$ . This sudden change in the rate of cells entering the system explains the kink in Figure 5.3.

In principle, it is possible to prolong the first stage of consistent and directed migration by iterating adding more cell types. Biologically speaking on the other hand, it is impossible for the neural tube to generate an infinite number of different cell types, all producing different chemicals. However, since cell migration always occurs over finite distances, only a finite number of cell types would be necessary to reach a specific target.

Alternatively, the chain model presented here can be considered as an abstraction of a cell to cell interaction where cells are simultaneously guiding and being guided, and where the signals do not only provide directional cues but also modify particular aspects of their behaviour on a spectrum, which we have reduced to discrete subpopulations.

# Chapter 6

## Conclusions

In this dissertation, we aimed to construct a PDE model for cranial neural crest cell migration based on recent insights that revealed an underlying leader–follower dynamic, as described in Chapter 1. We first discussed different chemotactic models in Chapter 2, where we showed that biological constraints do not permit chemotactic migration based on forced chemoattractant gradients, but rather that cell migration must rely on cell-induced gradients.

We then analysed a chemotactic model with a single cell type in Chapter 3 that satisfies the constraint of a cell-induced gradient, but was unrealistic in one of its other assumptions. Specifically, we showed that the cells would need to become infinitely sensitive to chemoattractant gradients as the chemoattractant concentrations approached zero. Due to biological limitations on chemotaxis, and the discrete nature of molecules, such an assumption is invalid for biological and physical reasons.

Nevertheless, the analysis provided valuable insight with respect to non-singular chemotaxis in long-distance migration. Essentially, a non-singular chemotactic law limits the range of cell-induced chemotaxis as the sensitivity becomes approximately constant for low chemoattractant concentrations, at which point the gradient is too shallow to provide directionality to the cell. This leads to a transition point behind the migrating cells where diffusion dominates over chemotaxis, which results in cells dropping out of the chemotactic front.

Chapter 4 addresses this issue by introducing a follower cell type that does not respond to the chemoattractant directly, but rather trails the leading cell type by a direct or indirect interaction, where the leading cells pursue a cell-induced chemoattractant gradient as before. However, we showed that this mechanism does not work if the cells are fixed in their roles. Instead, we demonstrated that it is crucial that the cells are able to switch their type based on their relative position within the

wave. With relatively simple rules, we showed that the population self-organises into a structure that increases the directionality of the population as a whole. These observations agree with experimental evidence that the leader and follower phenotypes are able to interconvert in the neural crest [1].

The advantage of the leader–follower model comes from leader cells converting to a different type of cell when they lag behind, as opposed to being lost to random motion as in the single cell type model. In Chapter 5, we demonstrated that this principle can be applied iteratively to obtain a coherent and directed cell stream of any length. Therefore, our model suggests the possibility that the neural crest cell stream is not composed solely of leaders and followers, but an array of cell types that maintain direction by a cascade of leader–follower interactions. Intriguingly, recent research, conducted after the formulation of the leader–follower model, has shown that the neural crest cells express a spectrum of different genes along the migratory pathway, indicating that our hypothesis is at least plausible.

# Appendix A

## Parameters

Table A.1: Parameters for forced chemoattractant gradient simulations for minimal model and receptor model in Figure 2.4.

| Symbol                | Description   | Value      |
|-----------------------|---|------------|
| Common parameters     |   |            |
| $T$                   | Simulated time  | 20         |
| $L$                   | Length of the domain  | 80         |
| $D_u$                 | Diffusion coefficient of leader cells                                   | 2          |
| $a$                   | Slope of forced chemoattractant gradient                                | $\sqrt{2}$ |
| $k$                   | Chemotactic coefficient in minimal and receptor model                   | $\sqrt{2}$ |
| Receptor model        |   |            |
| $\beta$               | Saturation parameter  | 0.5        |
| Simulation parameters |   |            |
| $\Delta t$            | Timestep in Crank–Nicolson scheme                                       | 0.1        |
| $N$                   | Number of first-order Lagrange elements used for spatial discretisation | 200        |

Table A.2: Parameters for leader model with naive boundary conditions in Figure 3.1.

| Symbol                | Description   | Value      |
|-----------------------|---|------------|
| $T$                   | Simulated time  | 100        |
| $L$                   | Length of the domain  | 150        |
| $D_u$                 | Diffusion coefficient of leader cells                                   | 1          |
| $D_c$                 | Diffusion coefficient of chemoattractant                                | 4          |
| $k$                   | Chemotactic coefficient of leader cells                                 | 2          |
| $\alpha$              | Consumption constant  | $\sqrt{2}$ |
| $u_-$                 | Leader density at $x = 0$   | $\sqrt{2}$ |
| $c_+$                 | Initial chemoattractant concentration                                   | $\sqrt{2}$ |
| Simulation parameters |   |            |
| $\Delta t$            | Timestep in Crank–Nicolson scheme                                       | 0.1        |
| $N$                   | Number of first-order Lagrange elements used for spatial discretisation | 300        |



Table A.3: Parameters for direct leader–follower model without and with conversion in Figure 4.1.

| Symbol                | Description   | Value     |
|-----------------------|---|-----------|
| $T$                   | Simulated time  | 300       |
| $L$                   | Length of the domain  | 175       |
| $D_u$                 | Diffusion coefficient of leader cells                                   | 2         |
| $D_v$                 | Diffusion coefficient of follower cells                                 | 2         |
| $D_c$                 | Diffusion coefficient of chemoattractant                                | 3         |
| $k_u$                 | Chemotactic coefficient of leader cells                                 | 5         |
| $k_v$                 | Chemotactic coefficient of follower cells                               | 5         |
| $\beta_u$             | Saturation parameter of leader cells                                    | $10^{-2}$ |
| $\beta_v$             | Saturation parameter of follower cells                                  | $10^{-2}$ |
| $\alpha$              | Consumption constant  | 0.1       |
| $n_{\max}$            | Maximum cell density at neural tube                                     | 1         |
| $b$                   | Steepness parameter in non-crowding cell flux                           | 20        |
| $g$                   | Base cell flux in non-crowding cell flux                                | 0.3       |
| $k_f$                 | Rate constant for transition from leaders to followers                  | 0.2       |
| $c_f$                 | Threshold concentration for transition from leaders to followers        | 0.05      |
| $k_g$                 | Rate constant for transition from followers to leaders                  | 0.1       |
| $c_g$                 | Threshold concentration for transition from followers to leaders        | 0.3       |
| Simulation parameters |   |           |
| $\Delta t$            | Timestep in Crank–Nicolson scheme                                       | 0.05      |
| $N$                   | Number of first-order Lagrange elements used for spatial discretisation | 250       |

Table A.4: Parameters for indirect leader–follower model in Figure 4.7.

| Symbol                | Description   | Value     |
|-----------------------|---|-----------|
| $T$                   | Simulated time  | 800       |
| $L$                   | Length of the domain  | 400       |
| $D_u$                 | Diffusion coefficient of leader cells                                   | 2         |
| $D_v$                 | Diffusion coefficient of follower cells                                 | 2         |
| $D_c$                 | Diffusion coefficient of chemoattractant                                | 3         |
| $D_a$                 | Diffusion coefficient of secondary chemoattractant                      | 3         |
| $k_u$                 | Chemotactic coefficient of leader cells                                 | 5         |
| $k_v$                 | Chemotactic coefficient of follower cells                               | 5         |
| $\beta_u$             | Saturation parameter of leader cells                                    | $10^{-2}$ |
| $\beta_v$             | Saturation parameter of follower cells                                  | $10^{-2}$ |
| $\alpha_c$            | Consumption constant of chemoattractant                                 | 0.1       |
| $\alpha_a$            | Consumption constant of secondary chemoattractant                       | 0.1       |
| $n_{\max}$            | Maximum cell density at neural tube                                     | 1         |
| $b$                   | Steepness parameter in non-crowding cell flux                           | 20        |
| $g$                   | Base cell flux in non-crowding cell flux                                | 0.3       |
| $k_f$                 | Rate constant for transition from leaders to followers                  | 0.2       |
| $c_f$                 | Threshold concentration for transition from leaders to followers        | 0.05      |
| $k_g$                 | Rate constant for transition from followers to leaders                  | 0.1       |
| $c_g$                 | Threshold concentration for transition from followers to leaders        | 0.3       |
| Simulation parameters |   |           |
| $\Delta t$            | Timestep in Crank–Nicolson scheme                                       | 0.05      |
| $N$                   | Number of first-order Lagrange elements used for spatial discretisation | 250       |

Table A.5: Parameters for chain model in Figure 5.1.

| Symbol                | Description   | Value     |
|-----------------------|---|-----------|
| $T$                   | Simulated time  | 3000      |
| $L$                   | Length of the domain  | 1000      |
| $D_u$                 | Diffusion coefficient of cells  | 2         |
| $D_c$                 | Diffusion coefficient of chemoattractant                                | 3         |
| $k_u$                 | Chemotactic coefficient of cells  | 5         |
| $\beta_u$             | Saturation parameter of cells   | $10^{-2}$ |
| $\alpha$              | Consumption constant  | 0.1       |
| $r$                   | Production constant   | 0.5       |
| $u_{\max}$            | Maximum cell density at neural tube                                     | 1         |
| $c_{\max}$            | Maximum chemoattractant concentration                                   | 1         |
| $b$                   | Steepness parameter in non-crowding cell flux                           | 20        |
| $g$                   | Base cell flux in non-crowding cell flux                                | 0.3       |
| $k_f$                 | Rate constant for transition from leaders to followers                  | 0.2       |
| $c_f$                 | Threshold concentration for transition from leaders to followers        | 0.05      |
| $k_g$                 | Rate constant for transition from followers to leaders                  | 0.1       |
| $c_g$                 | Threshold concentration for transition from followers to leaders        | 0.3       |
| Simulation parameters |   |           |
| $\Delta t$            | Timestep in Crank–Nicolson scheme for $N \neq 9$                        | 1         |
| $\tilde{\Delta} t$    | Timestep in Crank–Nicolson scheme for $N = 9$                           | 0.5       |
| $N$                   | Number of first-order Lagrange elements used for spatial discretisation | 1000      |

# References

- [1] R. McLennan, L. Dyson, K. W. Prather, J. A. Morrison, R. E. Baker, P. K. Maini, and P. M. Kulesa, “Multiscale mechanisms of cell migration during development: theory and experiment,” *Development*, vol. 139, no. 16, pp. 2935–2944, 2012.
- [2] R. McLennan, L. J. Schumacher, J. A. Morrison, J. M. Teddy, D. A. Ridenour, A. C. Box, C. L. Semerad, H. Li, W. McDowell, D. Kay, P. K. Maini, R. E. Baker, and P. M. Kulesa, “Neural crest migration is driven by a few trailblazer cells with a unique molecular signature narrowly confined to the invasive front,” *Development*, vol. 142, no. 11, pp. 2014–2025, 2015.
- [3] S. F. Gilbert and M. J. F. Barresi, *Developmental Biology*. Sunderland: Sinauer Associates, 11th ed., 2016.
- [4] E. Theveneau and R. Mayor, “Neural crest delamination and migration: From epithelium-to-mesenchyme transition to collective cell migration,” *Developmental Biology*, vol. 366, no. 1, pp. 34–54, 2012.
- [5] J. D. Murray, *Mathematical Biology I: An Introduction*. Berlin: Springer-Verlag, 3rd ed., 2002.
- [6] J. D. Murray, *Mathematical Biology II: Spatial Models and Biomedical Applications*. Berlin: Springer-Verlag, 3rd ed., 2003.
- [7] L. Dyson, P. K. Maini, and R. E. Baker, “Macroscopic limits of individual-based models for motile cell populations with volume exclusion,” *Physical Review E*, vol. 86, no. 3, 2012.
- [8] Abitua, “Neural crest formation during neurulation,” 2010. [https://commons.wikimedia.org/wiki/File:Neural\\_Crest.png](https://commons.wikimedia.org/wiki/File:Neural_Crest.png) [accessed: 2017-08-10].

- [9] P. Kulesa, D. L. Ellies, and P. A. Trainor, “Comparative analysis of neural crest cell death, migration, and function during vertebrate embryogenesis,” *Developmental Dynamics*, vol. 229, no. 1, pp. 14–29, 2004.
- [10] A. J. Trevenack and K. A. Landman, “A traveling wave model for invasion by precursor and differentiated cells,” *Bulletin of Mathematical Biology*, vol. 71, no. 2, pp. 291–317, 2009.
- [11] K. A. Landman, M. J. Simpson, and D. F. Newgreen, “Mathematical and experimental insights into the development of the enteric nervous system and Hirschsprung’s Disease,” *Development Growth and Differentiation*, vol. 49, no. 4, pp. 277–286, 2007.
- [12] W. Li and G.-A. Keller, “VEGF nuclear accumulation correlates with phenotypical changes in endothelial cells,” *Journal of Cell Science*, vol. 113, no. 9, pp. 1525–1534, 2000.
- [13] T. Hillen and K. J. Painter, “A user’s guide to PDE models for chemotaxis,” *Journal of Mathematical Biology*, vol. 58, no. 1-2, pp. 183–217, 2009.
- [14] D. Horstmann, “From 1970 until present : the Keller-Segel model in chemotaxis and its consequences,” *Jahresbericht der Deutschen Mathematiker-Vereinigung*, vol. 105, no. 3, pp. 103–165, 2003.
- [15] Z.-A. Wang, “Mathematics of traveling waves in chemotaxis,” *Discrete and Continuous Dynamical Systems - Series B*, vol. 18, no. 3, pp. 601–641, 2013.
- [16] E. F. Keller and L. A. Segel, “Traveling bands of chemotactic bacteria: a theoretical analysis,” *Journal of Theoretical Biology*, vol. 30, no. 2, pp. 235–248, 1971.
- [17] MrPomidor, “An illustration of the Weber–Fechner law,” 2017. [https://commons.wikimedia.org/wiki/File:Weber-Fechner\\_law\\_demo\\_-\\_dots.png](https://commons.wikimedia.org/wiki/File:Weber-Fechner_law_demo_-_dots.png) [accessed: 2017-08-22].
- [18] C. Xue, H. J. Hwang, K. J. Painter, and R. Erban, “Travelling waves in hyperbolic chemotaxis equations,” *Bulletin of Mathematical Biology*, vol. 73, no. 8, pp. 1695–1733, 2011.
- [19] S. C. Brenner and L. R. Scott, *The Mathematical Theory of Finite Element Methods*. New York: Springer, third ed., 2008.

- [20] P. Farrell, “Lecture Notes for C6.4 Finite Element Method for PDEs,” 2017. <https://courses.maths.ox.ac.uk/node/183> [accessed: 2017-04-20].
- [21] A. Logg, K.-A. Mardal, and G. N. Wells, *Automated Solution of Differential Equations by the Finite Element Method*, vol. 84. Springer, 2012.
- [22] M. S. Alnaes, J. Blechta, J. Hake, A. Johansson, B. Kehlet, A. Logg, C. Richardson, J. Ring, M. E. Rognes, and G. N. Wells, “The FEniCS project version 1.5,” *Archive of Numerical Software*, vol. 3, 2015.
- [23] L. Tweedy, D. A. Knecht, G. M. Mackay, and R. H. Insall, “Self-generated chemoattractant gradients: attractant depletion extends the range and robustness of chemotaxis,” *PLoS Biology*, vol. 14, no. 3, pp. 1–22, 2016.
- [24] E. F. Keller and L. A. Segel, “Initiation of slime mold aggregation viewed as an instability,” *Journal of Theoretical Biology*, vol. 26, no. 3, pp. 399–415, 1970.
- [25] T. Höfer, J. A. Sherratt, and P. K. Maini, “Dictyostelium discoideum: cellular self-organisation in an excitable medium,” *Proceedings of the Royal Society London B*, vol. 259, no. 1356, pp. 249–257, 1995.
- [26] T. Pak, *Numerical analysis of Fisher’s equation in FEniCS*. Special topic, University of Oxford, 2017.
- [27] C. Johnson and V. Thomée, “Error estimates for some mixed finite element methods for parabolic type problems,” *RAIRO: Numerical analysis*, vol. 15, no. 1, pp. 41–78, 1984.
- [28] V. Thomée, *Galerkin Finite Element Methods for Parabolic Problems*. Berlin Heidelberg: Springer-Verlag, 2nd ed., 2006.
- [29] H. Chen, R. Ewing, and R. Lazarov, “Superconvergence of mixed finite element methods for parabolic problems with nonsmooth initial data,” *Numerische Mathematik*, vol. 78, no. 4, pp. 495–521, 1998.